This is a repository copy of *Two-phase SPH Simulation of Fluid-Structure Interactions*.

Two-phase SPH Simulation of Fluid-Structure Interactions

Kai Gong[1], Songdong Shao[2], Hua Liu[3, *], Benlong Wang[3] and Soon-Keat Tan[4]

[1] Tropical Marine Science Institute, National University of Singapore, 18 Kent Ridge Road, Singapore 119227. Email: gkfly@hotmail.com

[2] Department of Civil and Structural Engineering, University of Sheffield, Sheffield S1 3JD, United Kingdom. Email: s.shao@sheffield.ac.uk (State Key Laboratory of Hydro-Science and Engineering, Tsinghua University, Beijing 100084, China; School of Water Resources and Electric Power, Qinghai University, Xining 810016, China)

[3] Department of Engineering Mechanics, Shanghai Jiao Tong University, Shanghai 200240, China

[4] NEWRI and Maritime Research Centre, School of Civil and Environmental Engineering, Nanyang Technological University, Nanyang Avenue, Singapore 639798. Email: ctansk@ntu.edu.sg

[*] Correspondence author, Email: hliu@sjtu.edu.cn

Abstract

In this paper, a two-phase Smoothed Particle Hydrodynamics (SPH) method is used to simulate the fluid-structure interactions with violent deformation of the free surface. An improved solid boundary treatment is proposed based on the accurate pressure interpolations of the inner fluid particles. The model performance is validated by sloshing in a water tank and dam break flow impact on a vertical wall. In the practical model applications, a two-dimensional wedge entry into the static water is studied, for which the flow fields of water and air phases are computed simultaneously. It has been found that both the water flow around the wedge cavity and the air flow inside are reasonably predicted. Also the two-phase model has been found to accurately provide the flow features throughout the entire entry process, while the single-phase model can only predict the flows before the closure of the cavity due to the lack of air modelling. Besides, a laboratory experiment on the wedge entry has also been carried out for the validation purposes.

Keywords:

SPH; two-phase; solid boundary; fluid-structure interaction; air cavity; wedge entry.

Introduction

Fluid-structure interactions are an important topic in the design and operation of coastal and offshore facilities. The accurate prediction of the flow fields as well as the structure responses could provide useful information to the industry. For example, the water entry is a typical fluid-structure impact problem which occurs in the field of marine hydrodynamics. Following the pioneering work of von Karman, quite a few research studies have been carried out to examine the hydrodynamic features during the entry process, such as the deformation of free surface, evolution of the cavity region, fluid impact force and motion of the falling object (Wang et al., 2013; 2015). Early research works were mostly based on the analytical and experimental methods, such as reported by Zhao and Faltinsen (1993).

Since the interactions between the fluid and structure usually lead to the large free surface deformation and wave breaking, the numerical models based on the partial differential hydrodynamic equations, i.e. Navier-Stokes (N-S) equations, demonstrate their unique advantages of being able to provide the detailed flow information without the limitation imposed in the laboratory experiment and field observation. For example, Lin (2007) solved the Reynolds-averaged N-S equations for the study of water entry of a circular cylinder. In recent years, the mesh-free Smoothed Particle Hydrodynamics (referred as SPH) method becomes quite attractive in simulating the violent deformation of free surface and the wave breaking. As a result, a variety of fluid-structure interaction problems have been investigated by using either SPH (Gao et al., 2012; Liu et al., 2014; Ren et al., 2014) or other similar mesh-free particle models (Koshizuka et al., 1998; Hwang et al., 2014). SPH was originally developed for the astrophysical computations by Gingold and Monaghan (1977) and later modified to model the fluid flows by Monaghan (1994). It is a pure Lagrangian particle method which does not need the grid to calculate the spatial derivatives. Instead, this is achieved by the analytical differentiation of the interpolation functions. Therefore, the continuity and momentum conservation equations are formulated as a set of ordinary differential equations, and the SPH particle positions and attributes are computed by using the standard numerical integration methods in the time domain. With regard to the water entry problem, there exist quite a few good SPH works including Vandamme et al. (2011), Skillen et al. (2013) and Liu et al. (2014). It has been found that the SPH method is quite promising in simulating these kinds of transient impact problems and very refined flow features can be captured by the mesh-free particle motion. For instance, Oger et al. (2005; 2006) pioneered the SPH application of water entry problems and showed that accurate solid boundary treatment is a key to the realistic simulation of wedge kinematics and dynamics. Besides, Maruzewski et al. (2010) extended the work to a much larger engineering scale using the HPC simulation.

Solid boundary treatment and air-phase modeling should be carefully examined to accurately predict the fluid motion and structural response during the fluid-structure interaction process. Both of them strongly influence the impact pressure and force on the structure and thus on its motion. For the water entry problems, for instance, the air cavity enclosed by the water could significantly affect the flow field and the hydrodynamic loading. The early multi-phase SPH modelling concept was proposed by Monaghan and Kocharyan (1995) for the compressible flows. Later substantial works have been implemented by Hu and Adams (2006; 2007) and Grenier et al. (2009) using more advanced solutions to treat the mass conservation and the interface stability. One promising improvement in the free surface flow simulations we follow here was made by Colagrossi and Landrini (2003), who proposed a straightforward and efficient two-phase model for the large density ratios and tested the model on a variety of benchmark cases. Besides, the robust treatment of solid boundary conditions is also quite important, especially for the boundaries surrounding the moving structure. The repulsive boundary (Monaghan, 1994) provided a simple treatment of the solid wall to prevent particle penetrations, but it could cause the pressure oscillations in the fluid region. The mirroring boundary (Cummins and Rudman, 1999) could be the most accurate one but it was achieved at the expense of the CPU time, and also the numerical program could become heavy for the complex boundary configurations. The so-called dynamic boundary (Gómez-Gesteira and Dalrymple, 2004) provided an alternative way to treat the solid boundary with economic computing time.

In this paper, we will further explore the two-phase water-air modelling concept of Colagrossi and Landrini (2003), and combine it with an improved solid boundary treatment from Gómez-Gesteira and Dalrymple (2004) to study the fluid-structure interactions including the challenging water entry of a wedge based on the study of Oger et al. (2006). In the previous works by the same authors (Gong et al., 2009; 2010), we investigated the early stage of the water entry by using a single-phase SPH model and found that there was almost no difference in the simulation results whether a single-phase or a two-phase model was used. One main objective of the present work is to investigate more in-depth hydrodynamics during the entire wedge entry process with the support of our own laboratory experiment. Prior to this, we will use two benchmark tests to validate the model accuracy, including the sloshing in a water tank and the dam break flow impact on a solid wall with air-cushion effect.

Here it should be noted that our present two-phase SPH model is only applicable to the low-speed entry problems. This is due to that in the more challenging high-speed water entry of 10 ~ 20 m/s, the compressibility of water could become significant and the severe cavitations could lead to the complex phase changes, so more advanced SPH models should be developed to account for these effects. Besides, the flow turbulence should be taken into consideration by studying various turbulence closure techniques (Violeau and Issa, 2007). However, most established turbulence models were based on the steady flow state and more investigations should be made to examine their validity in such a transit flow condition like

the wedge entry. Also, the Reynolds scaling would provide an elegant approach to address these similar problems and make the relevant connections on different flow scenarios. Finally, we should be aware of a recent group of accurate techniques to treat the solid boundaries based on the boundary integrals, e.g. Kulasegaram et al. (2004) and De Leffe et al. (2009). This kind of approach has proved to be very accurate, although computationally expensive, and has been extended to the frictional forces and turbulence by Ferrand et al. (2010, 2012), to the incompressible SPH (ISPH) by Leroy et al. (2014) and to the thermal fluxes by Leroy et al. (2015). Our present model is less expensive than these boundary integral techniques, but it has the limitations when applied to other kinds of wall boundary condition such as the Neumann.

Principles of Two-phase SPH Model

The governing equations of the fluid dynamics follow the Navier-Stokes (N-S) equations. Assuming the fluid viscosity being not dominant, the shear stresses can be ignored and the following continuity and momentum equations are often used in the SPH representations:

$$\frac{\mathrm{d}\rho}{\mathrm{dt}} = -\rho \nabla \cdot \mathbf{u} \tag{1}$$

$$\frac{d\mathbf{u}}{dt} = -\frac{1}{\rho} \nabla P + \mathbf{g} \tag{2}$$

where ρ is the fluid particle density; t is the time; $\mathbf{u}$ is the particle velocity vector; P is the pressure; and $\mathbf{g}$ is the gravitational acceleration.

There are various forms of the SPH formulation for the above governing equations and they demonstrate both advantages and disadvantages depending on the different hydrodynamic applications. In this paper we investigate the influence of air cavity during the violent fluid-structure interactions, so the revised SPH representations by Colagrossi and Landrini (2003) are used in the computations. The continuity equation is therefore formulated by SPH as

$$\frac{\mathrm{d}\rho_a}{\mathrm{dt}} = \rho_a \sum_{b=1}^{N} \frac{m_b}{\rho_b} \mathbf{u}_{ab} \cdot \nabla_a W_{ab} \tag{3}$$

where a is the reference particle and b represents the neighbouring particle; m_b is the particle mass; $\mathbf{u}_{ab} = \mathbf{u}_a - \mathbf{u}_b$ is the velocity difference between the two particles; W is the SPH interpolation kernel function and $\nabla_a W_{ab}$ represents the gradient of kernel taken with respect to particle a ; and N is the number of particles for the summation. In this work, the cubic spline kernel normalized in 2D (Monaghan, 1994) is used. According to our previous

computational experience this kernel has the compact support, good accuracy and reasonable computational cost. Recently it has been found that the Wendland kernel performs much better and avoids quite a few tensile instabilities (Dehnen and Aly, 2012; Ferrand et al., 2012), which should be tested in future studies. To avoid instability on the two-phase interface, the following pressure gradient representation is used for Equation (2)

$$\frac{1}{\rho}(\nabla P)_a = \sum_{b=1}^{N} m_b (\frac{P_a + P_b}{\rho_a \rho_b}) \nabla_a W_{ab} \tag{4}$$

The standard weakly compressible SPH formulation adopts the following Equation of State to compute the fluid pressure, thus avoiding the solution of a pressure Poisson matrix

$$P = B[(\frac{\rho}{\rho_0})^\gamma - 1] \tag{5}$$

where $\gamma = 7$ and $\rho_0 = 1000$ kg/m^3 are used for the water. The constant B is related to the sound speed c_0, which is about ten times or more larger than the highest bulk flow velocity and calculated by $B = c_0^2 \rho_0 / \gamma$. In a two-phase flow simulation with large density differences, Colagrossi and Landrini (2003) recommended a background pressure χ to be added to avoid the tensile instability. Meanwhile, an artificial cohesion force should also be included for the light fluid phase in order to obtain a clear two-phase interface. So the finally adopted pressure equation reads

$$P = B[(\frac{\rho}{\rho_0})^\gamma - 1] + \chi - \bar{a} \rho^2 \tag{6}$$

where $\bar{a}$ represents the surface tension effect and this term is not considered in the present study. The recent study by Violeau and Leroy (2014) found that the use of a background pressure could have serious consequence on the stability of SPH computations, which is reflected by the fact that an increase in the background pressure would lead to a decrease in the computational time step. In this work, we have not done extensive sensitivity analysis on this and we simply gave 1000 pa as the background pressure for both the phases. What we have found was that too small a value could lead to the negative pressures and too large a value could cause the pressure noises.

In the SPH numerical scheme, $\prod_{ab}$ is an artificial viscosity term that increases the stability properties of the algorithm. It has the following form as:

$$\prod_{ab} = \begin{cases} -\alpha \frac{\bar{c}_{ab}}{\bar{\rho}_{ab}} \mu_{ab} & \mathbf{u}_{ab} \cdot \mathbf{r}_{ab} < 0 \\ 0 & otherwise \end{cases} \tag{7}$$

5

where α is a dimensionless coefficient and its value depends on the different applications as shown later in the computational cases. The bar values represent the average of relevant variables for particles a and b ; and $\mathbf{r}_{ab} = \mathbf{r}_a - \mathbf{r}_b$ is the difference in spatial locations between the two particles. μ_{ab} is calculated by a modified form of Colagrossi and Landrini (2003) for the two-phase water-air flow as

$$\mu_{ab} = h\frac{k_a + k_b}{2}\frac{\mathbf{u}_{ab} \cdot \mathbf{r}_{ab}}{\mathbf{r}_{ab}^2 + \eta^2} \tag{8}$$

where h is the kernel smoothing distance, which represents the range of particle interactions and is taken as the multiple of the initial particle spacing; η is a small number to prevent the singularity; and k is defined as

$$k_a = \frac{|\nabla \cdot \mathbf{u}_a|}{|\nabla \cdot \mathbf{u}_a| + \sqrt{\mathbf{S}_a : \mathbf{S}_a} + 10^{-4}c_a / h} \tag{9}$$

where $\mathbf{S}$ is the rate-of-strain tensor and $\mathbf{S} : \mathbf{S}$ is the tensor operation defined in Colagrossi and Landrini (2003).

So the final SPH momentum equation adopted in the computations becomes

$$\frac{d\mathbf{u}_a}{dt} = -\sum_{b=1}^{N} m_b(\frac{P_a + P_b}{\rho_a \rho_b} + \Pi_{ab})\nabla_a W_{ab} + \mathbf{g} \tag{10}$$

The SPH time integration is carried out based on the following frog-leap schemes as:

$$\rho^{n+1/2} = \rho^{n-1/2} + (\frac{d\rho}{dt})^n \frac{\Delta t^{n-1} + \Delta t^n}{2} \tag{11}$$

$$\mathbf{u}^{n+1/2} = \mathbf{u}^{n-1/2} + (\frac{d\mathbf{u}}{dt})^n \frac{\Delta t^{n-1} + \Delta t^n}{2} \tag{12}$$

$$\mathbf{r}^{n+1} = \mathbf{r}^n + \mathbf{u}^{n+1/2}\Delta t^n \tag{13}$$

where n indicates the time variable. The computational time step Δt is constrained by the following CFL condition as

$$\Delta t = CFL \cdot \min(\frac{h_a}{c_a + |\mathbf{u}_a|}) \tag{14}$$

where CFL is a dimensionless coefficient 0.0 ~ 1.0. Recently Violeau and Leroy (2014) found that different time integration schemes could have important effects on the numerical performance.

Besides, in the SPH computations the standard XSPH invariant (Monaghan, 1994) is used to regularize the particle motions and a first-order interpolation scheme based on the Moving-Least-Square principle (Colagrossi and Landrini, 2003) is used to re-initialize the density field every 20 time steps to improve the consistency between the mass, density and occupied volume during the simulations.

Improved Solid Boundary Treatment

The accurate treatment of the solid boundary conditions is important for evaluating the impact pressure and force during the fluid-structure interactions. The dynamic boundary originally proposed by Gomez-Gesteira and Dalrymple (2004) provided a robust way to deal with this issue. In this approach, the boundary particles share some properties of the inner fluid particles and follow the continuity equation and the equation of state, but their velocities are zero and their positions are kept unchanged. Therefore, the computational treatment of the system is considerably simplified. In this paper, we propose an improvement on the original dynamic boundary method, in which the boundary particles also have the properties of the inner fluid particles, but the pressures of these boundary particles are obtained by interpolating the pressures of the inner fluid particles in the vicinity of solid wall. There are several advantages using this treatment. Firstly, it is not necessary to make a prior assumption on the nature of the force exerted by the solid boundary such as used in the reflective boundary method (Monaghan, 1994). Secondly, the computational procedure is quite simple as there is no need to mirror the fluid particles across the boundary like that used by Cummins and Rudman (1999). Thirdly, the computed flow fields are much more reasonable because the boundary pressure is close to the "exact" pressure. Finally, the non-penetration boundary conditions can also be well maintained.

Here the pressure of the boundary particles is obtained by using the following procedure. As shown in Fig. 1, for a given boundary particle B, its pressure is obtained by interpolating the pressures of the fluid particles in the near boundary area around B (within the S_{sensor} area). Only the fluid particles which are within a distance d from the boundary (which is proportional to the smoothing length) contribute to the pressure at point B. First, we project the fluid particles onto the nearby boundary area, and the pressure of the projected point is obtained from the fluid particle pressure as well as the hydrostatic component of the pressure related to its vertical distance to the projection point. Then we divide the boundary area into n parts whose characteristic length is proportional to the smoothing length. Assuming the

area of the i th part is dS_i and the pressure P_i at this part is the averaged pressure of all projected points within dS_i, then the final pressure P_B at particle B is calculated as

$$P_B = \frac{\sum_i^n P_i dS_i}{\sum_i^n dS_i} \qquad (15)$$

Similarly, the pressures of all boundary particles are obtained in this way and then used to solve the momentum equations for the neighbouring fluid particles.
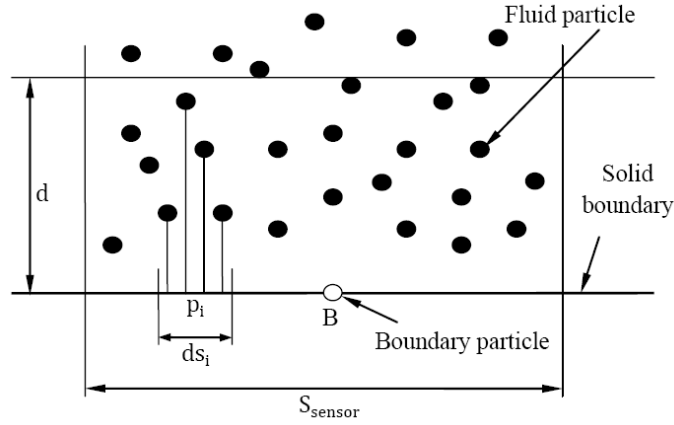
Fig. 1 Schematic view of improved solid boundary treatment

The above interpolation method is similar to that proposed by Oger et al. (2006). However, several differences exist in our improved approaches. For instance, Oger's interpolation was only used to obtain the pressure of some points on the solid boundary and the global boundary treatment still followed the mirror particle rule. Another advantage of our improved approach is that the contribution of all particles can be reasonably reflected by use of the arithmetic averaging even when two or more inner fluid particles occupy the same projection point, while some kinds of the underestimation or overestimation could occur in Oger's treatment. Finally, our proposed method is also computationally efficient since the boundary projection segment dS_i is uniformly distributed within S_{sensor} and thus it is time-independent. However, we should realize that our pressure projection of the fluid particles to the boundary is in nature simply an addition of the hydrostatic pressure ($P_b = P_a + \rho g(y_a - y_b)$), assuming fluid particle a is projected to boundary point b), but this approach ignores any variation in the dynamic pressure which is quite important for the fluid impact problems. In our computations, we have used a vertical projection distance d = 3h in Fig. 1, and thus the boundary conditions are first-order accurate in the particle spacing dx, which should improve with the spatial convergence. Besides, it should also be pointed out that Mayrhofer et al. (2013) proposed a similar formulation as Eq. (15) to deal with more challenging Neumann boundary. The advantage of using Eq. (15) over the standard SPH interpolations arises from the fact that more reasonable numerical results could be obtained near the solid boundary.

Model Validations and Result Analysis

In this section, we will use two benchmark tests to validate the proposed model improvement in the solid boundary treatment and two-phase formulation, using the sloshing in a water tank and the dam break flow impact on a vertical wall.

Sloshing in a water tank

To validate the solid boundary treatment, here a nonlinear sloshing in a smooth rectangular tank due to the horizontal surge excitation is simulated by using the improved model without the air phase. The computational results are compared with the experimental data of Faltinsen et al. (2000). Also, the comparisons are made with the computations by using the standard dynamic boundary to show the model improvement. The computational water tank is shown in Fig. 2, with the tank height, length and initial water depth being 1.05 m, 1.73 m and 0.6 m, respectively. A wave gauge is placed in the position of 0.05 m from the left wall to monitor the water surface displacement.
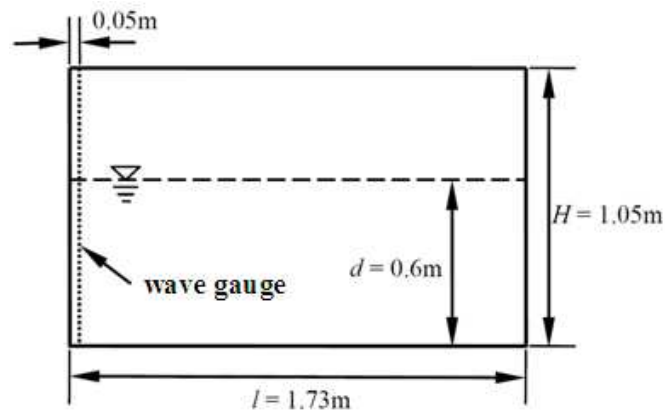
Fig. 2 Schematic setup of sloshing water tank

Two different particle spacing are used, i.e. $\Delta X = 0.01$ m and 0.005 m, to examine the convergence of the model and the effect of improved boundary treatment. For $\Delta X = 0.005$ m, a total of 41520 fluid particles are used with 3366 boundary particles. The fixed computational time step is $\Delta t = 5 \times 10^{-5}$ s. A sloshing simulation of 50 s cost nearly 120 CPU hours on a typical desktop (CPU Athlon 64 2.1GHz). The density of water is $\rho = 1000$ kg/m^3, artificial viscosity coefficient $\alpha = 0.01$, XSPH coefficient $\varepsilon = 0.1$ and EoS constant $B = 100000$.

The computed time histories of the water surface levels at the wave gauge are shown in Fig. 3 (a) and (b), respectively, for the results before and after the solid boundary improvement. It is shown that the improved computations are insensitive to the choice of particle spacing and almost identical water surface profiles are obtained for the two different particle sizes, while the standard boundary treatment leads to a larger discrepancy in the two numerical results.
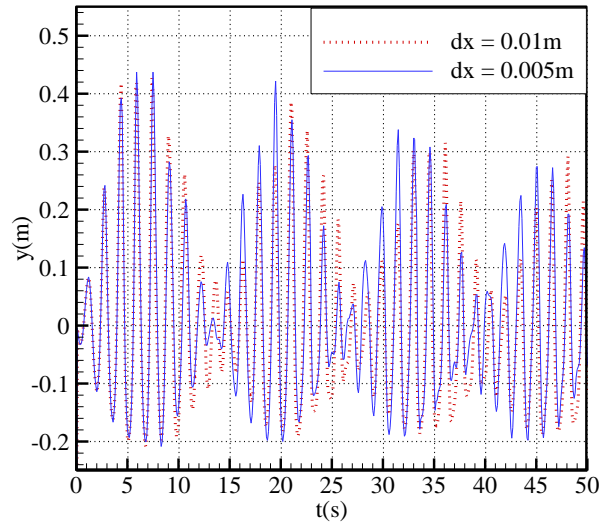
(a)
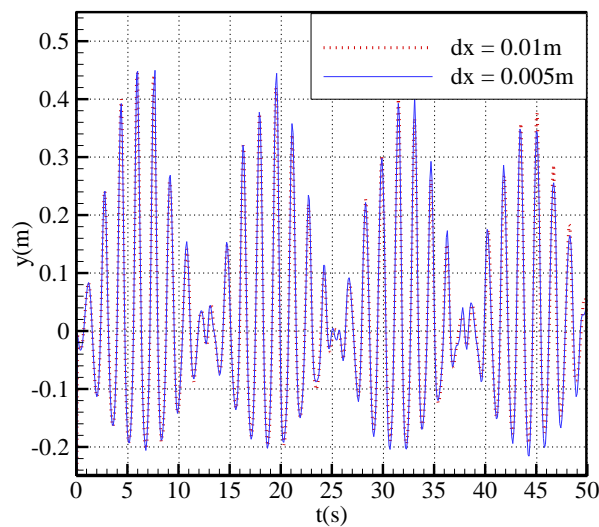
(b)

Fig. 3 Computed time histories of water surface profiles by using (a) standard boundary treatment; and (b) improved boundary treatment

To examine the improved boundary treatment, Fig. 4 (a) and (b) show the snapshots of the flow field computed based on the standard and improved boundary treatment, respectively, at time t = 20.2 s. It is shown in Fig. 4 (a) that the standard boundary treatment leads to relatively higher numerical dissipations and the fluid particles near the left boundary are stuck to the solid wall while those near the right wall are repelled from it. The reason is due to that the pressures of the boundary particles have been obtained by solving the SPH continuity equation and the equation of state. During this process, only half of the fluid particles in the support domain contributed to the boundary particles due to the truncation of the kernel. In comparison, in the improved computations as shown in Fig. 4 (b), the boundary pressures have been interpolated from the fluid particles directly and thus they are not linked to the kernel function of the boundary particles.
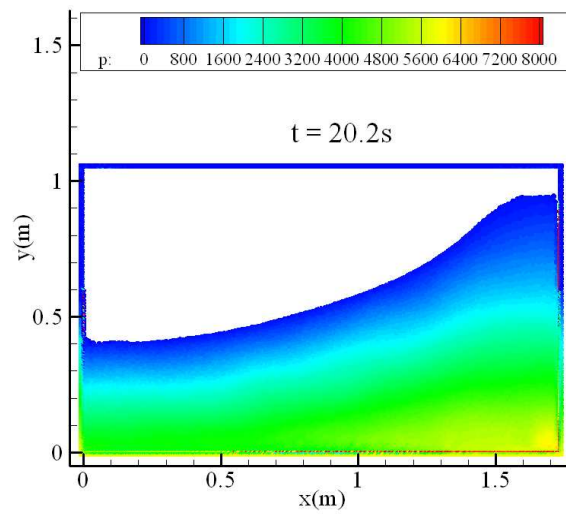
(a)
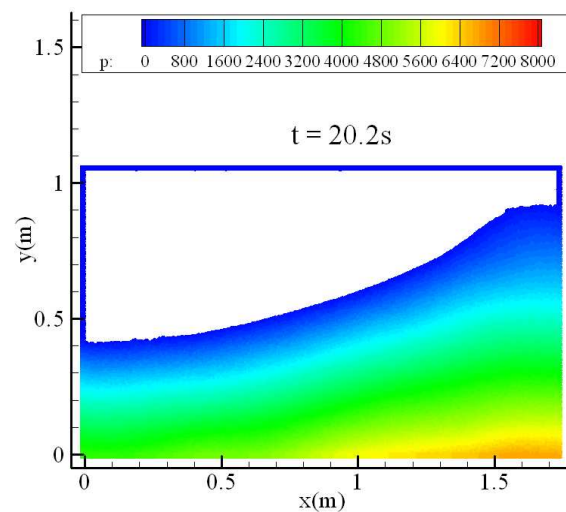
(b)

Fig. 4 Snapshots of computed flow field for (a) standard boundary treatment; and (b) improved boundary treatment (pressure unit: pa)

To validate the accuracy of the SPH computations, Fig. 5 (a) and (b) show the comparisons of the computed time histories of free surface elevations with the experimental results of Faltinsen et al. (2000), for two different boundary treatments. It can be seen that both the amplitude and phase period of the modulated waves computed by using the improved boundary treatment are in a better agreement with the experimental observations, whereas the results obtained from the standard boundary approach decrease rapidly with time as a result of the numerical dissipation. The effect of improvement is much more obvious for the smaller wave profiles around time t = 12 ~ 14 s, 25 ~ 28 s and 37 ~ 40 s.
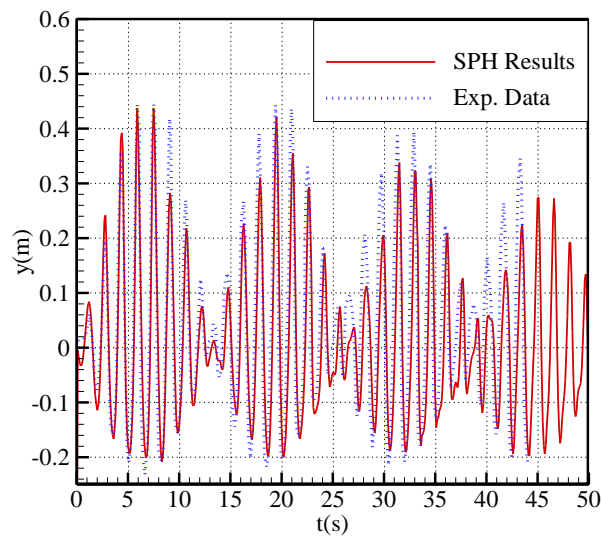
(a)
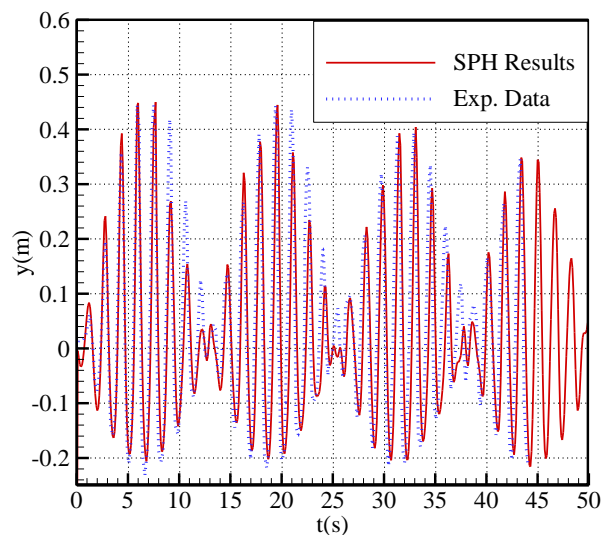
(b)

Fig. 5 Comparisons of SPH computed free surface elevations with experimental data of Faltinsen et al. (2000) for (a) standard boundary treatment; and (b) improved boundary treatment

To further demonstrate our improvement in the pressure predictions on the solid boundary, we also computed the sloshing case of Chen et al. (2013) and compared with their experimental data and SPH computations using an advanced coupled dynamic solid boundary. The schematic setup of the sloshing tank is shown in Fig. 6, with the tank breadth B = 1 m, tank height H = 1 m and initial water depth d = 0.3 m. The tank is rolled at the center of the bottom following a sinusoidal motion. The first natural frequency and rolling period of the sloshing system is ω_0 = 4.76 rad/s and T_0 = 1.32 s. In the present SPH simulations, we use two external excitation frequencies of ω = 0.95 rad/s and 3.09 rad/s, respectively. A pressure sensor is located at a position of 0.2 from the left corner of the tank to measure the fluid impact pressures.
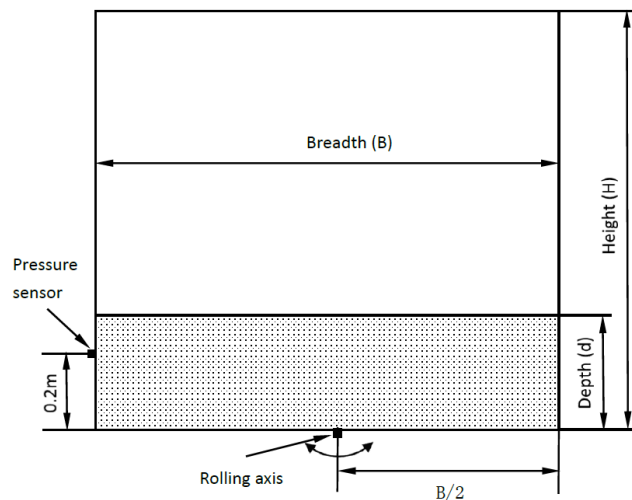
Fig. 6 Schematic setup of sloshing water tank for pressure validation

The SPH computational parameters are used as follows: EoS coefficient B = 100000, artificial viscosity coefficient α = 0.01 and particle spacing ΔX = 0.005 m with 12000 fluid particles and 2430 boundary particles in the computational system. A constant time step of $\Delta t = 5 \times 10^{-5}$ s is used for the frog-leap time integration. Due to the accumulation of numerical dissipations as the time progresses, the experimental and numerical data were analyzed within the first 20 s of the simulation by following the recommendation of Chen et al. (2013). This cost about 50 hours of CPU time on a DELL workstation (CPU Intel X5675，3.0 GHz). Here it should be mentioned that the value of artificial viscosity coefficient α should influence the wave decay but we did not make sensitivity investigation on this.

Our SPH computed pressure time histories at the gauging point are compared with the experimental data of Chen et al. (2013) and their SPH results in Fig. 7 (a) and (b), for the two different excitation frequencies. Due to the existence of high frequency pressure oscillations, the present SPH simulation results have been processed by the noise filtering technique, which is detailed in the Appendix. In the SPH computations of Chen et al. (2013), they used an improved SPH model combining the modified Moving Least Squares (MLS) method for the density re-initialization and the advanced coupled dynamic solid boundary treatment for the accurate prediction of pressure on the solid boundary. Fig. 7 shows that our proposed

solid boundary model can much better capture the phase and amplitude of the impact pressure values at the measuring point, while the SPH computations of Chen et al. (2013) significantly under-predicted the pressures in case of the larger excitation frequency.
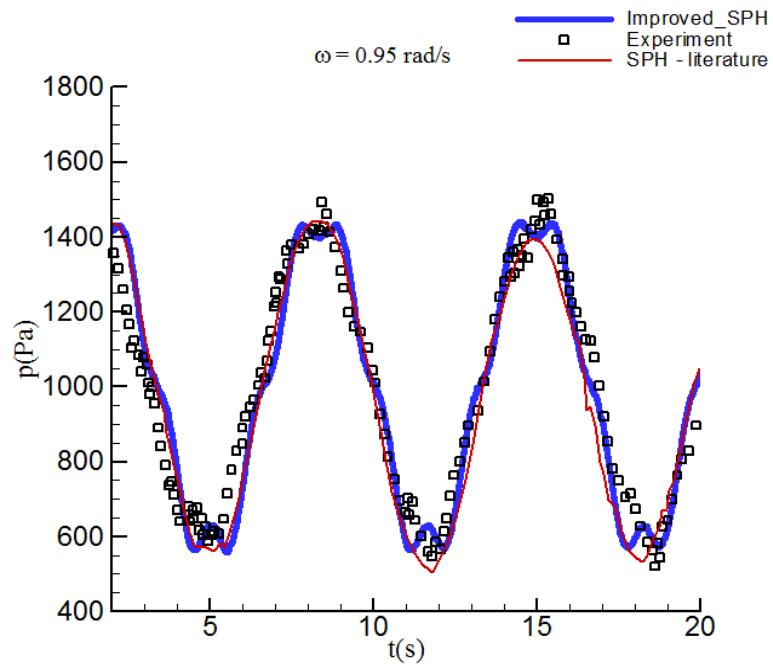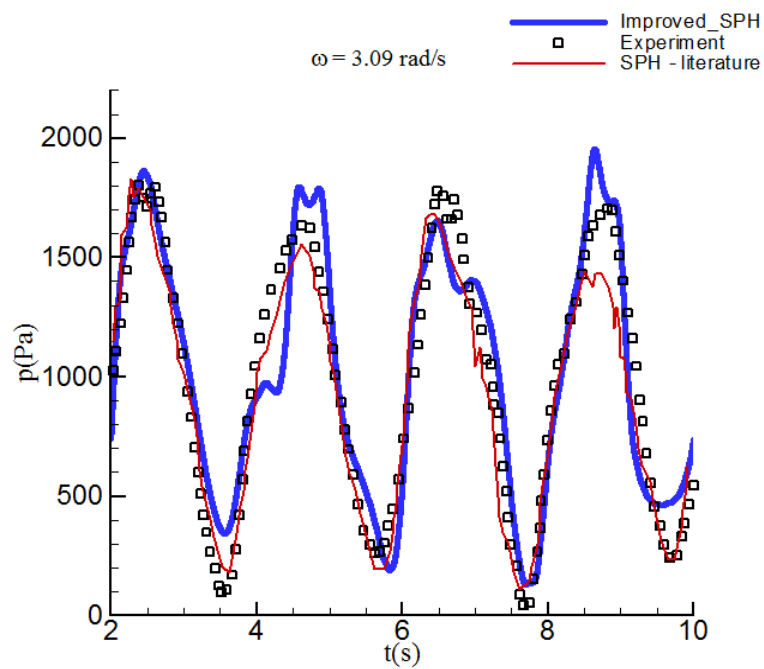
Fig. 7 Computed and measured time histories of impact pressure on the gauging point for excitation frequency of (a) $\omega = 0.95$ **rad/s; and (b)** $\omega = 3.09$ **rad/s**

Two-phase dam break flow impact on a vertical wall

In this section, the proposed two-phase SPH model with the improved solid boundary treatment is used to simulate a dam break flow impact on a vertical wall. As the flow impacts on the wall and then returns back to form a closed air cavity region, the single-phase SPH model is not expected to provide accurate result at this stage. Similar problem has also been addressed by Colagrossi and Landrini (2003). Here we revisit this case for two purposes, first to validate our improved boundary treatment scheme, second to demonstrate the two-phase model could provide better simulation results than the single-phase model.

The computational setup is shown in Fig. 8. Two water gauges and one pressure gauge are installed in the computational domain to monitor the time history of water levels and pressure variations used to validate the numerical model. The particle spacing is taken as $\Delta X = 0.01$ m, and there are totally 7200 water particles, 50760 air particles and 4080 boundary particles in the computational system. A variable time marching step is used and the CFL coefficient is 0.3. The simulation was executed to non-dimensional time scale $t(g/H)^{1/2} = 8$ using 320000 time steps and this cost about 170 CPU hours on a DELL T5400 workstation (CPU INTEL XEON E5420 2.5GHz). The density of the water and air is taken as 1000 kg/m^3 and 1 kg/m^3, respectively. The artificial viscosity coefficient is $\alpha = 0.03$, XSPH coefficient is $\varepsilon = 0.5$, EoS coefficient is $B = 2800000$ and background pressure is $\chi = 1000$ Pa for both the water and air phases. We have not attempted a sensitivity analysis on the background pressure but we found that too small a value could lead to the negative pressure and too large a value could cause the strong pressure noise. Here our selections of B and χ follow the benchmark work of Monaghan (1994) and Colagrossi and Landrini (2003).
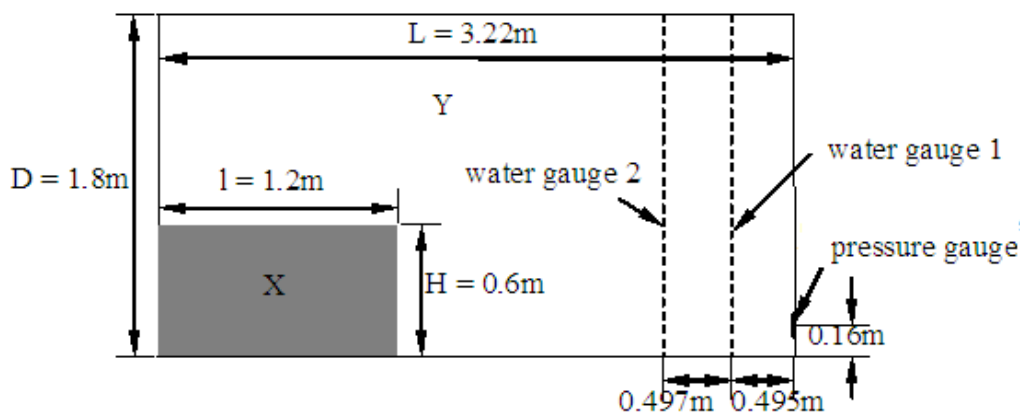
Fig. 8 Schematic setup of computational domain and gauge locations of dam break flow

To show the differences between the single- and two-phase SPH modelling, the SPH computed dam break flow snapshots are compared with the two-phase Level-Set results of Colicchio et al. (2003). The comparisons are shown in Fig. 9 for the four different time instants. It shows that for the normalized time $t(g/H)^{1/2} < 6.12$, when the air cavity region has not closed yet, there is almost no difference observed between the single- and two-phase SPH simulations. However, after the air cavity is enclosed at $\tau > 6.12$, the two-phase SPH computations agree much better with the Level-Set results of Colicchio et al. (2003) in predicting the shape and scale of the air cavity as well as the water jet. In comparison, the single-phase SPH computations have provided quite different flow patterns.
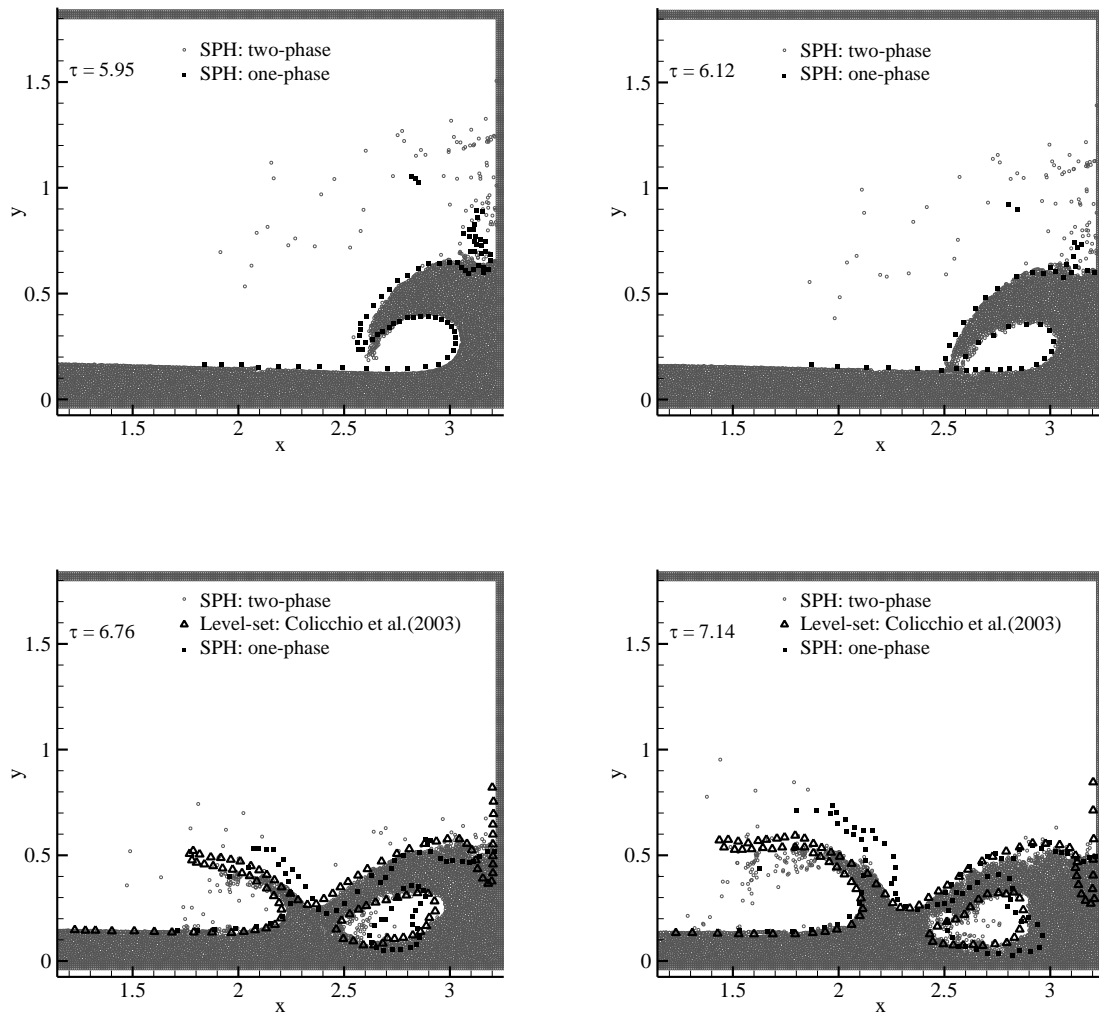
Fig. 9 Comparisons of single- and two-phase SPH computations with Level-Set results of Colicchio et al. (2003) for dam break flow (axis unit: m)

Fig. 10 shows the time history of water surface variations at gauge 1 and 2. The experimental and numerical results from Zhou et al. (1999) are also shown for a comparison. The observed hump in the water surface levels at the very beginning of the experiment (around $t(g/H)^{1/2}$

16

= 2 ~ 3 for gauge 1 and 1.4 ~ 2.3 for gauge 2) is due to the influence of air bubble being mixed with the leading front of flooding water on the measurement facilities, which is not found in the numerical results. Nonetheless, the SPH simulations are closer to the experimental data than the numerical results of Zhou et al. (1999). Afterwards, the dam break flow enters a relatively stable stage, for gauge 1 it is around $t(g/H)^{1/2}$ = 3.0 ~ 5.5 and it is 2.3 ~ 6.3 for gauge 2. This time corresponds to the stage when the dam break water flows over the water gauge, hits the right wall and starts to return back. The SPH results show very satisfactory agreement with the experiment while relatively larger errors are found in the numerical results of Zhou et al. (1999). However, when the returned flow passes over the water gauge again, some kinds of discrepancy are found between the SPH results and the experimental data at gauge 1, although there is still a good match with the numerical results of Zhou et al. (1999). Meanwhile, a much better agreement has been found at the water gauge 2 for the SPH predictions. Similar phenomena were also reported by Colagrossi and Landrini (2003), but it would be difficult to find the reason since no detailed information on the experiment was available from Zhou et al. (1999).
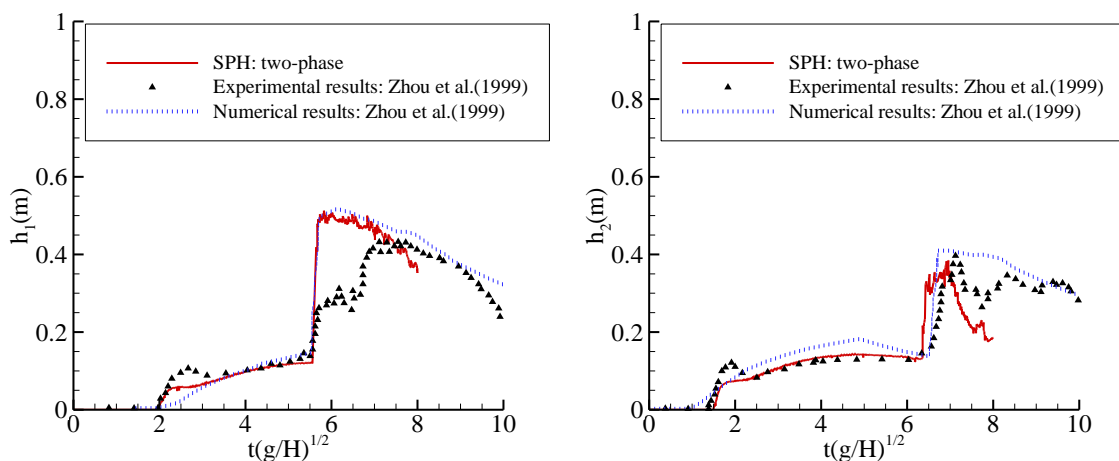
Fig. 10 Computed and measured time histories of water surface levels at gauge 1 (left) and gauge 2 (right)

Fig. 11 shows the time history of impact pressure of the dam break flow on the measurement point of the right wall. The SPH computations are also compared with the experimental and numerical results of Zhou et al. (1999). It shows that both the SPH and numerical results of Zhou et al. (1999) can well predict the rapid pressure increase when the dam break flow hits the right wall, but the SPH results seem to be closer to the experiment at the beginning of the impact. Besides, it is obvious around $t(g/H)^{1/2}$ = 6.0, when the returned flow from the right wall plunges onto the water surface and forms an air cavity area, that the SPH computations better reflect the pressure peak while the numerical computation of Zhou et al. (1999) significantly underestimated this value.
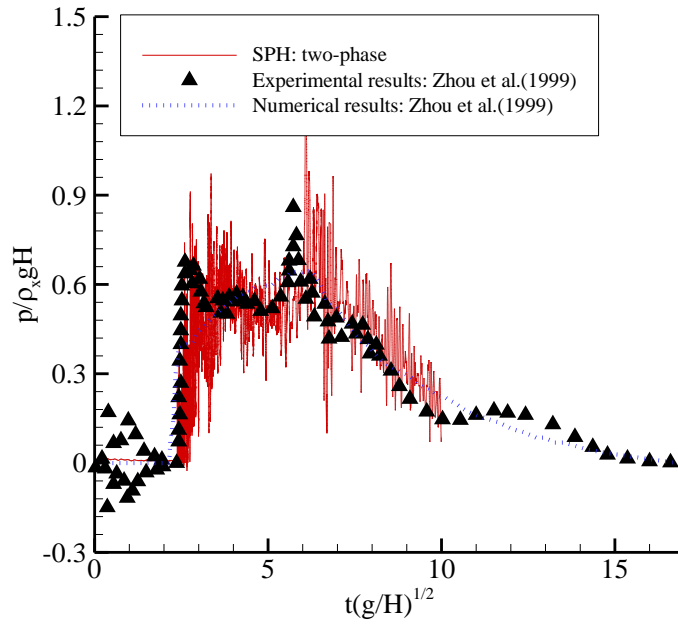
Fig. 11 Computed and measured time histories of impact pressures on the right wall

The reason Fig. 11 contains a lot of high frequency noises is due to that we have used a variable computational time-step in the SPH simulations and output the numerical data in an irregular time series. Our present data noise filtering tool can only process the numerical results at regular time intervals (see Appendix for more details). It should be noted that the novel work of Marrone et al. (2011) of using a density filtering in the continuity equation would be a great substitute for such smoothing techniques as the XSPH, density re-initialization and artificial viscosity etc, in view of improving the SPH prediction accuracy. However, in this study we only used the standard SPH smoothing treatments since the main objective is to demonstrate the improved solid boundary treatment and the superiority of the two-phase modelling. Although the pressure field in Fig. 11 looks noisy, the general evolution patterns can still be followed to provide a meaningful prediction.

Model Applications - Wedge Entry into the Water

In this section the proposed two-phase SPH model with the improved solid boundary treatment is used to study the wedge entry into the water. In the early stage of the wedge entry, it has been found that the single-phase SPH model could provide enough accuracy for the falling wedge dynamics and kinematics (Gong et al., 2009). So here we will focus on the later stage of the wedge entry when the air cavity near the wedge is closed, aiming to explore the differences between the single- and two-phase modelling approaches. Two wedge entry

studies will be carried out, one of which is based on the well-known benchmark work of Oger et al. (2006) and the other is based on our laboratory experiment.

Single- and two-phase SPH modelling of wedge entry of Oger et al. (2006)

The computational wedge and water tank settings are identical to those in Oger et al. (2006), except that the dimension of the present water tank is larger in order to accommodate long-time wedge entry simulations to study the later stage of the process. So the adopted water tank is 6.0 m long and the initial water depth is 4.0 m. The wedge entered into the water in the middle section of the tank with an entry velocity of 6.15 m/s. By considering the computational accuracy and efficiency, a particle spacing $\Delta X = 0.01$ m is used. As a result, there are 240,000 water particles and 7806 boundary particles in the computational system, while in the two-phase computations there are also 148,934 air particles. A fixed computational time step $\Delta t = 2 \times 10^{-6}$ s is used. In the study, one second of water entry simulation cost 40 CPU hours in the single-phase run and 100 CPU hours in the two-phase run by using a DELL T5400 Workstation (8 cores). The density of the water and air is taken as 1000 kg/m^3 and 1 kg/m^3, respectively. The artificial viscosity coefficient is $\alpha = 0.1$, XSPH coefficient $\varepsilon = 0.5$, EoS constant B = 700000 and background pressure 1000 pa for both the water and the air phases. Besides, an efficient sponge layer is placed on the lateral solid walls of the water tank to absorb undesirable reflection waves (Gong et al., 2009).

Fig. 12 shows the computed particle snapshots by the single- and two-phase SPH models (only the water particles are shown in the two-phase results) for the time instant of t = 0.1, 0.3, 0.5, 0.6, 0.7 and 0.9 s, respectively. It shows that before the enclosure of the air cavity region until t = 0.5 s, the influence of air on the wedge entry is negligible and thus there is almost no difference observed between the two modelling results. However, when the air cavity is closed from t = 0.6 s, due to the air pressure being zero in the single-phase model, the air cavity region is continuously compressed by the pressures of neighbouring water particles. As a result, a series of disturbance waves are generated from the contraction region. In comparison, the two-phase SPH computations include some levels of air pressure inside the cavity region, so the air region gradually shrinks and forms an air bubble moving together with the falling wedge. After the full closure of the water surfaces, strong flow jets are generated and the downward jet splits the air bubble into two symmetric parts. At this stage, the differences between the two modelling approaches are demonstrated not only by the movement of the air region but also by the water jet on the free surface and the free surface deformation. Here we should clarify that, in our low-speed entry wedge with a deep dead-rise angle, the air phase effect could be unimportant in the early stages of the process. However, for the entry problems with a low dead-rise angle, such as a plate, the air cushion can have a significant effect even at the impact. This has been supported by the study of Huera-Huarte et al. (2011) and Lind et al. (2015).

20
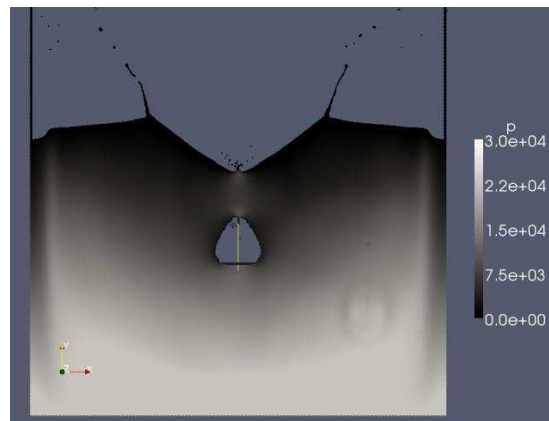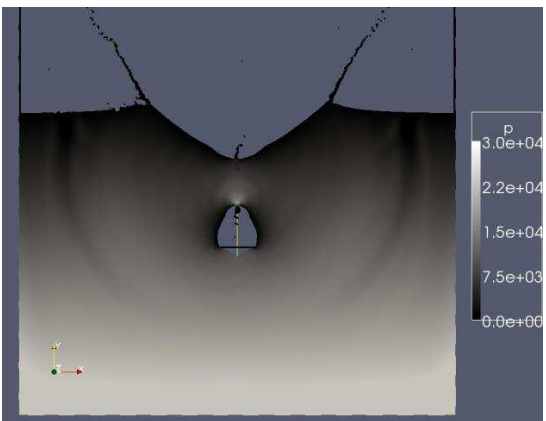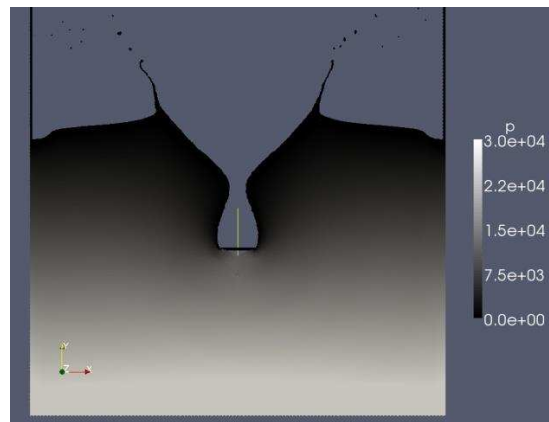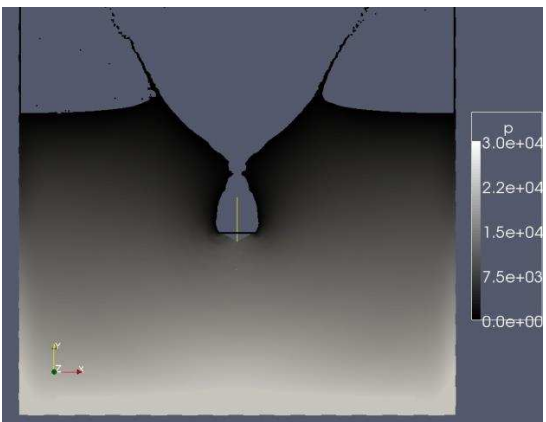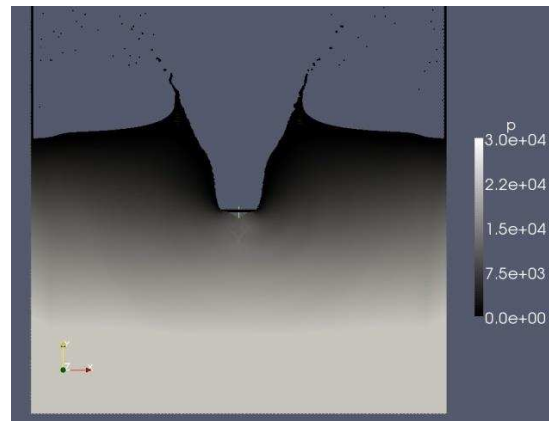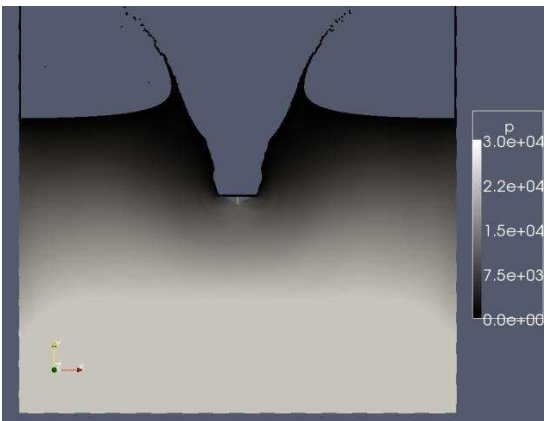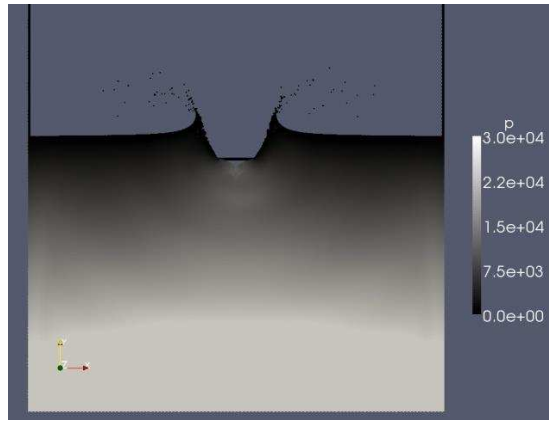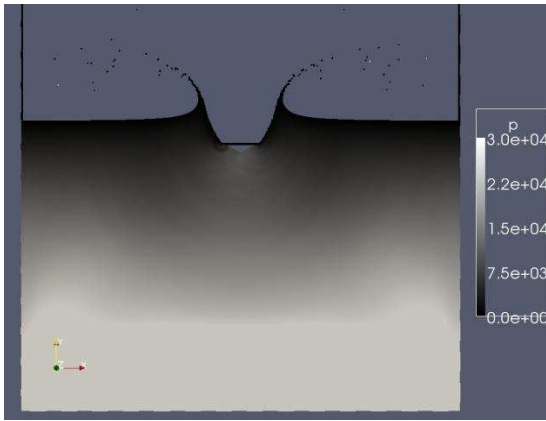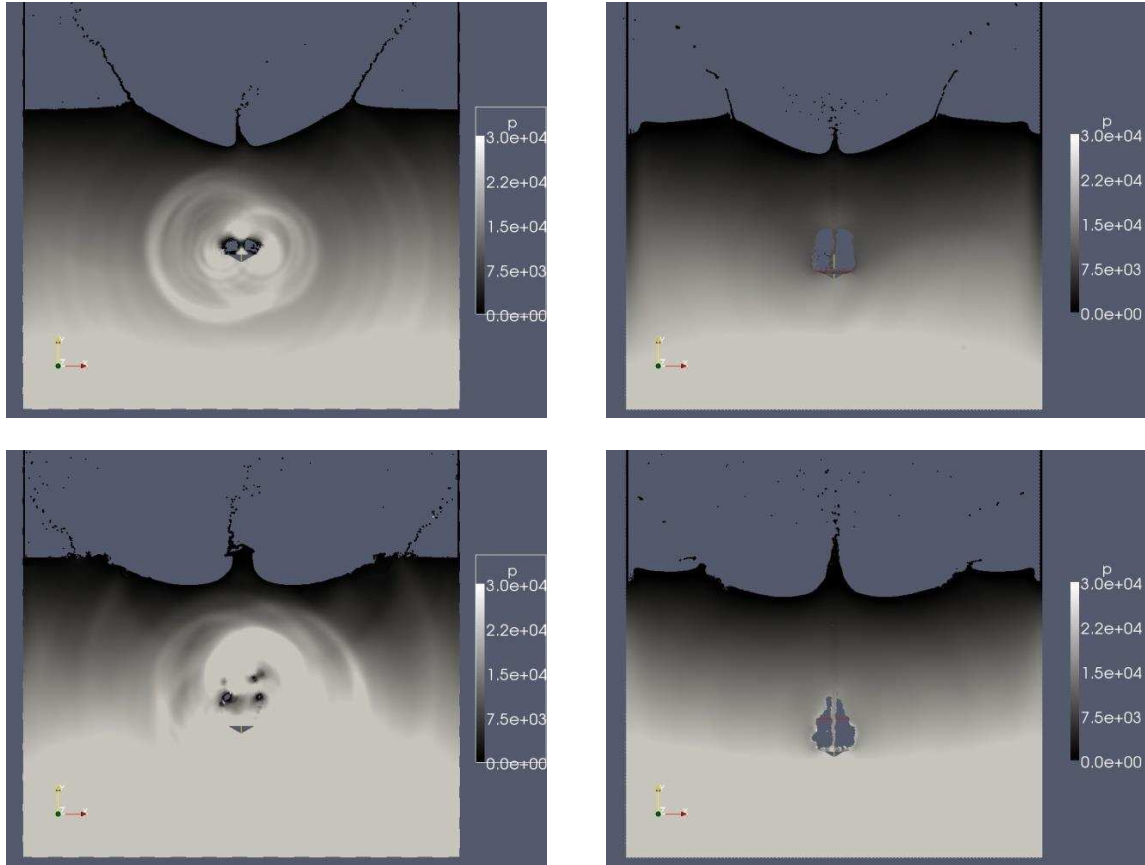
Fig. 12 Single- (left) and two-phase (right) SPH computations for wedge entry and air bubble evolutions, at t = **0.1, 0.3, 0.5, 0.6, 0.7 and 0.9 s (from up to down) (pressure unit: pa)**

In Fig. 12 we found that the two-phase descent velocity is slightly faster than the single-phase. Since there is neither experimental nor literature data available to support this, we plotted the time histories of falling velocities for the two numerical simulations in Fig. 13 aiming to explain this phenomenon. It is shown in Fig. 13 that at the beginning of the computation (t = 0.0 ~ 0.02 s), there is almost no difference in the falling velocity since the air pressure is zero in both the single- and two-phase computations. Before the enclosure of the air cavity (t = 0.02 ~ 0.55 s), the air pressures in the two-phase computation counteract with the wedge resistance to enable its falling velocity being faster. After the cavity enclosure up to the flow jet arrival on the wedge surface (t = 0.55 ~ 0.65 s), the existence of air pressure in the two-phase modelling continuously enlarges the velocity difference with the single-phase result. When the flow jet impacts on the wedge surface (t > 0.65 s), due to the collapse of the cavity region in the single-phase simulation which generated a series of disturbance waves, a slightly higher pressure appears on the wedge surface. As a result, the velocity differences between the single- and two-phase modelling results keep almost unchanged afterwards.
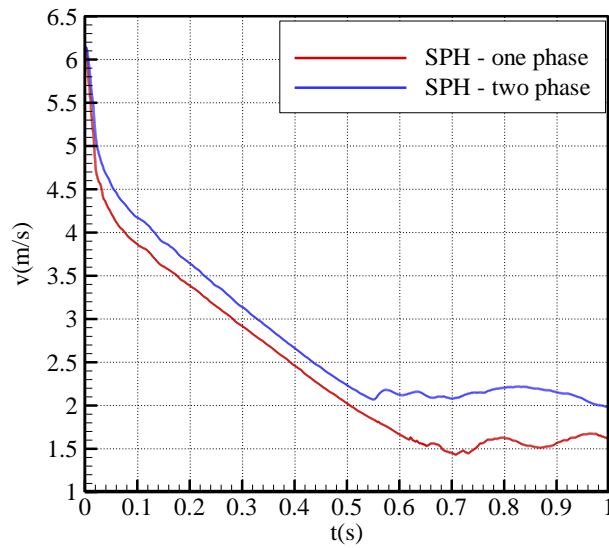
Fig. 13 Time histories of wedge falling velocity in single- and two-phase SPH computations

To further analyze the two-phase modelling results, Fig. 14 shows the velocity and pressure fields near the air cavity region at several time instants. It is shown that before the closure of the air cavity, such as time $t < 0.56$ s, the pressure of air region is still very small except on the very leading front. However, after the closure of the cavity region from $t > 0.56$ s, the pressure of the air region greatly increases and the two water columns near the cavity region collide with each other, which generated two strong flow jets moving in opposite vertical directions. The downward jet separates the air region into two independent ones and they move further down following the wedge motion.

t = **0.48 s**   t = **0.56 s**
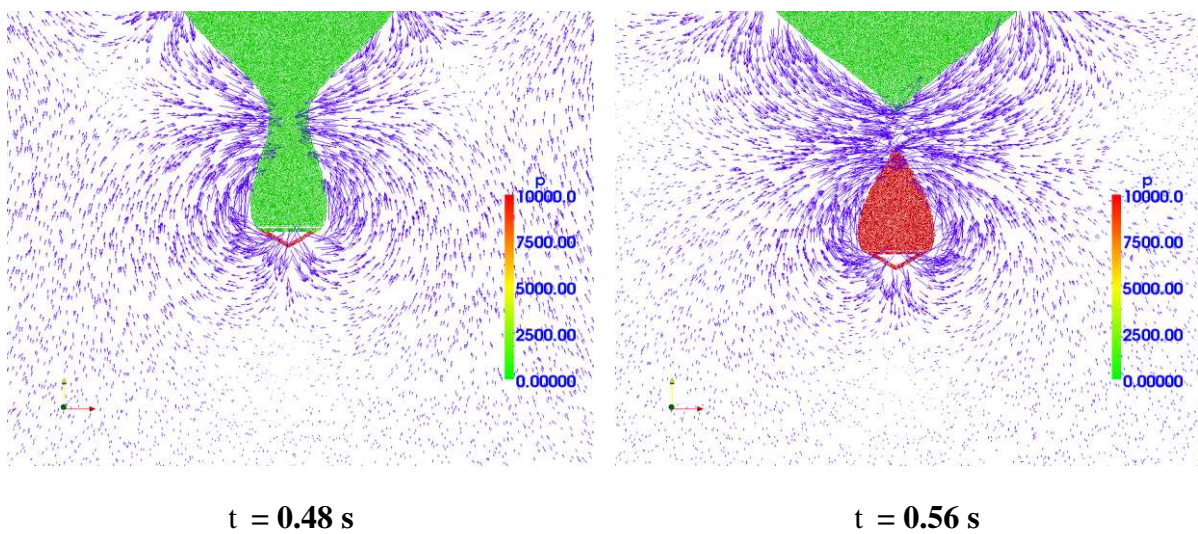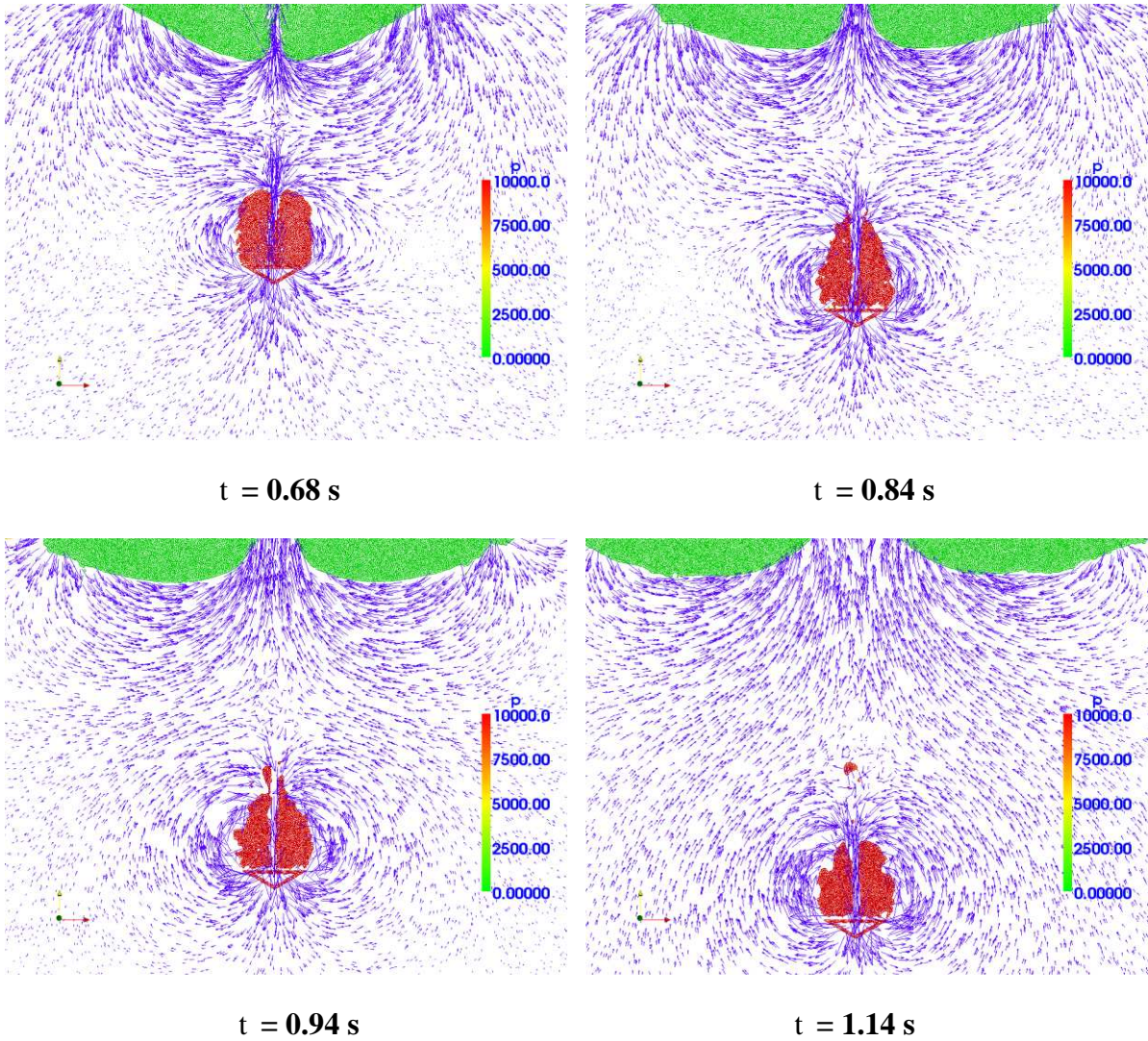
Fig. 14 Computed velocity and pressure fields near air cavity during wedge entry (pressure unit: pa)

Fig. 15 shows the localized pressure and velocity fields just before, on and after the closure of the air cavity region at time t = 0.548, 0.552 and 0.556 s, respectively, in which the black lines represent the water–air interface. It can be shown that before the closure of the air cavity at t = 0.548 s, the pressures of the air particles have already increased above the atmospheric values. This is due to that the connection route between the air cavity region and outside atmosphere becomes narrow and the compressed air inside cannot be completely released. This is also reflected by the corresponding velocity fields which indicate the rapid escape of air towards the water surface. Then during the cavity closure at t = 0.552 s and afterwards, the pressure inside the air region is larger than the surrounding water pressure. This pressure can balance the inertia force of the water phase during the shrinking of the air region, thus enable the air cavity to reduce in a stable manner.
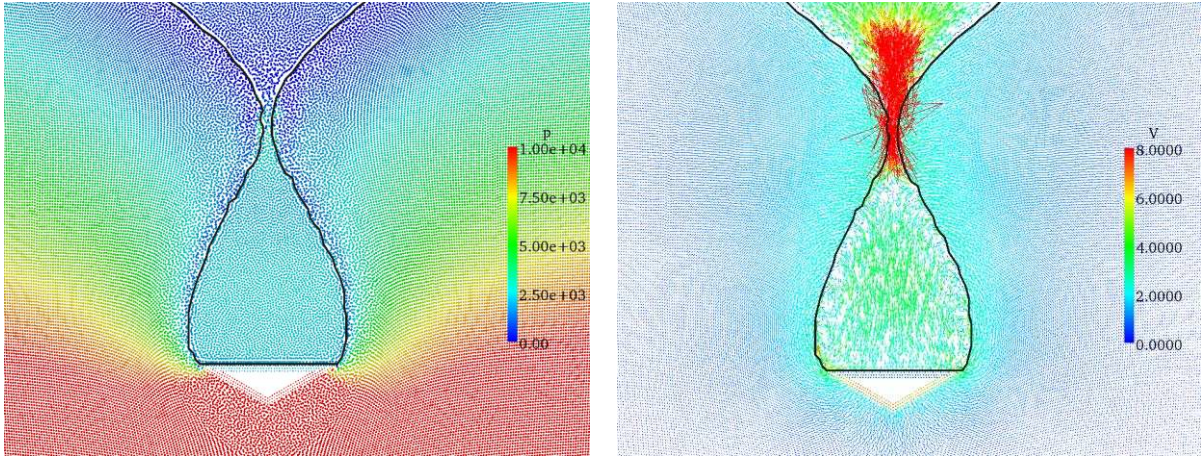
(a) t = **0.548 s**
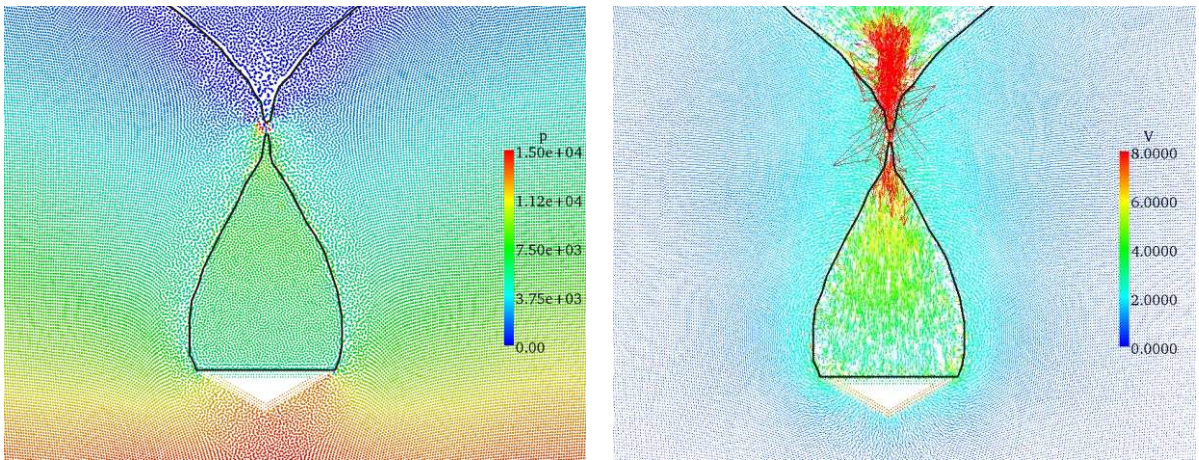
(b) t = **0.552 s**
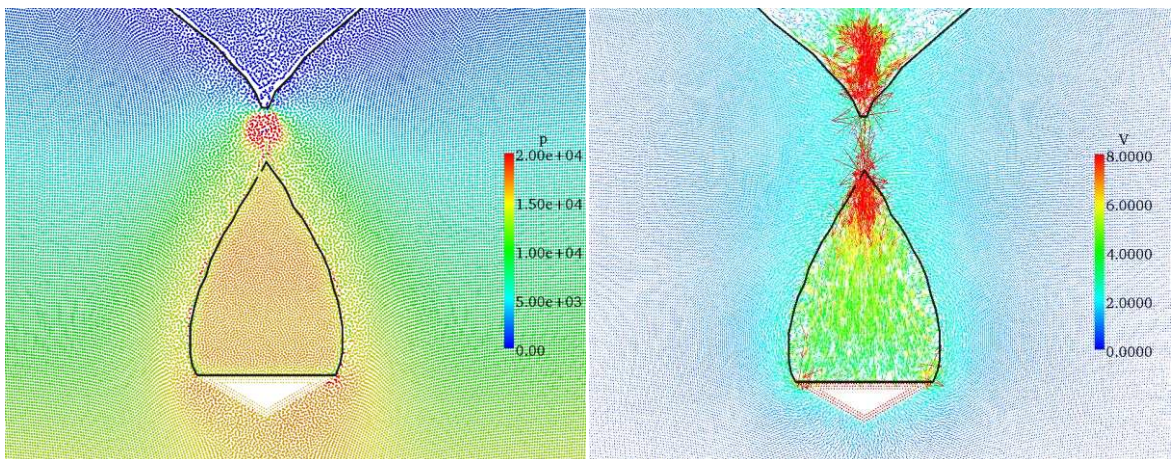
(c) t = **0.556 s**

Fig. 15 Computed pressure (left) and velocity (right) fields before (t = **0.548 s**), **on** (t = **0.552 s**) **and after** (t = **0.556 s**) **the closure of air cavity during wedge entry (pressure unit: pa; velocity unit: m/s)**

To investigate the pressure and volume changes of the air cavity region after the closure, the time series of computed snapshots and relative volume variations are shown in Figs. 16 and 17. It is found that the shrinking of the air cavity has caused the increase of air pressure, until to time t = 0.568 s, when the largest pressure peak is arrived and the cavity volume is minimum. Then the air cavity region starts to expand and the pressure inside is reduced accordingly, until to time t = 0.608 s, when the smallest pressure peak is found and the cavity volume is maximum. After that, there is a relatively stable short period of time during which the pressure and volume of the air cavity region remain almost the same. This corresponds to the time scale of t = 0.608 ~ 0.632 s. Then the air cavity shrinks again, leading to a second increase in the pressure and reduction in the air volume, until a peak value is reached at t = 0.672 s. The above expanding and shrinking processes continue alternatively until the intensity of both becomes smaller. It should be noted that the present model is based on the weakly compressible SPH assumption, which requires the density variation of the fluid being below 1%. The volume results in Fig. 17 indicate that the computed averaged volume change is around 1% and the maximum volume change is below 2%, thus justifying the use of the compressible model.
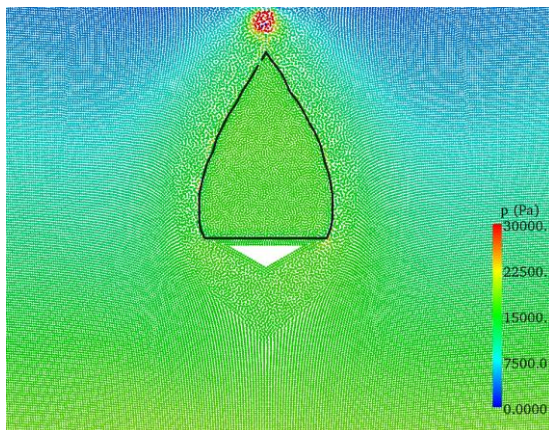
t = 0.556 s
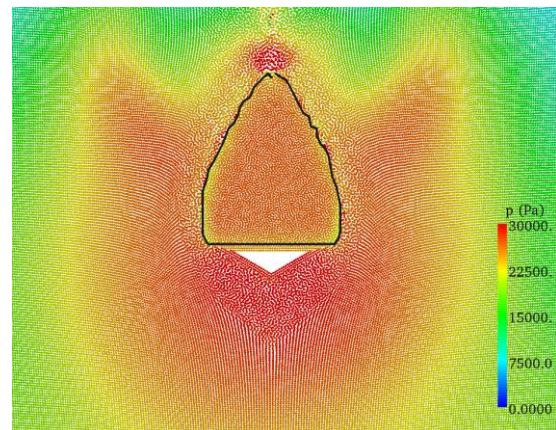
t = 0.568 s
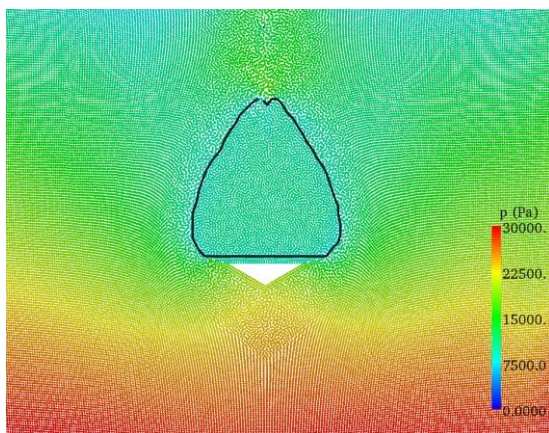
t = 0.588 s
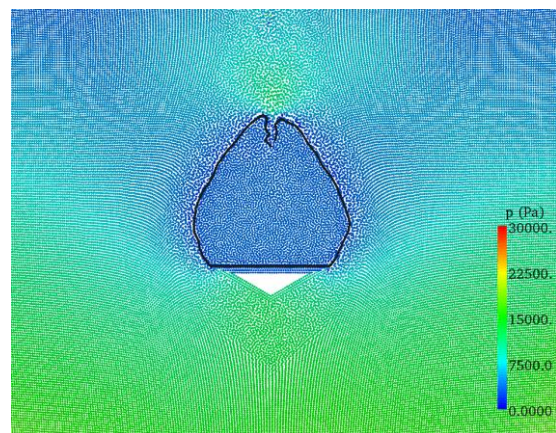
t = 0.608 s

t = **0.652 s**   t = **0.672 s**
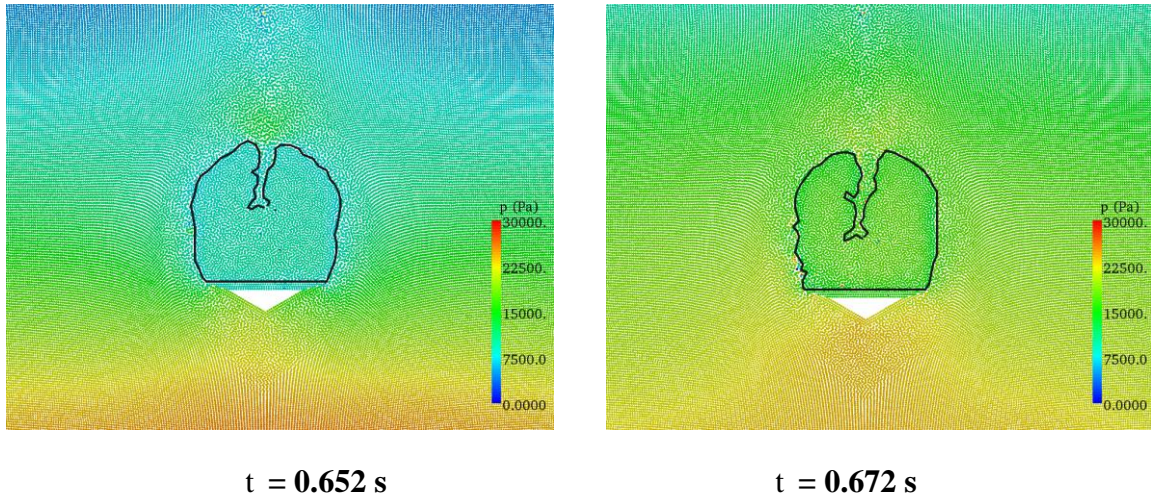
Fig. 16 Computed pressure fields after closure of air cavity during wedge entry
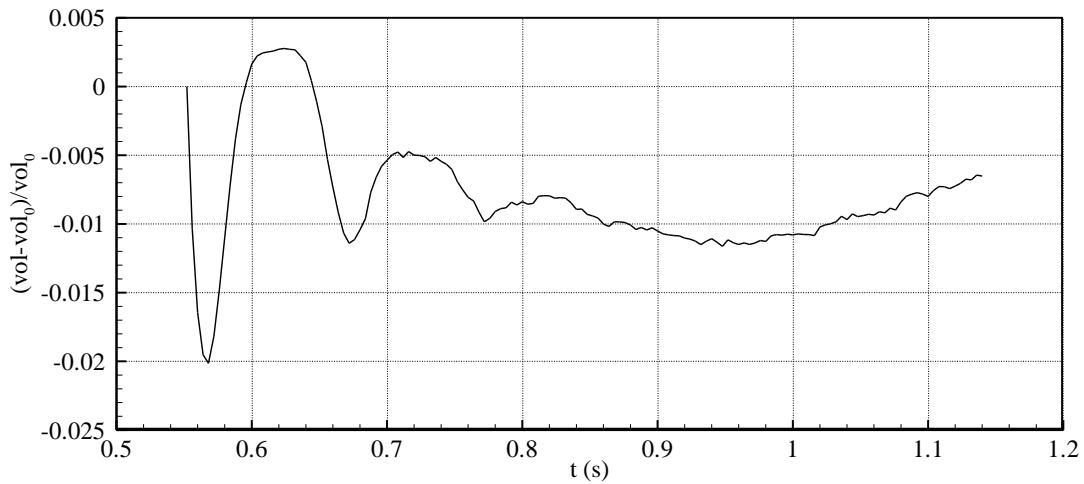
Fig. 17 Time histories of volume change of air cavity region after closure

To study the fluid drag forces on the falling wedge, Fig. 18 provides the time histories of the vertical drag forces during the entire wedge entry process. For clarity, the time axis has been split into three continuous stages. It shows that before the closure of the air cavity at t = 0.552 s, both the single- and two-phase SPH models predicted very similar drag forces. During the closure of air cavity around t = 0.552 ~ 0.575 s, due to the two-phase computations including the air pressure inside cavity region, the pressure force on the wedge surface has increased. As a result, the total vertical drag force computed by the two-phase model is smaller than that obtained from the single-phase model, for which the air pressure is constantly at zero and thus there is no reduction in the total vertical forces. After the complete closure of the air cavity from t = 0.575 s until to the end of the simulation, high frequency oscillations are found in the single-phase results due to the generation of disturbance waves from the contracted air region, while very mild variations have been found in the two-phase

results thanks to the damping effect of the air cushion inside the cavity area. We could explain this from Fig. 12 in that during the closure of the cavity, the single-phase computations produced very obvious pressure fluctuations due to the sudden collapse of the cavity region without the air pressure inside. On the other hand, the air bubble in the two-phase simulations balanced some external pressures to maintain the existence of the cavity region thus did not generate the pressure pulses.
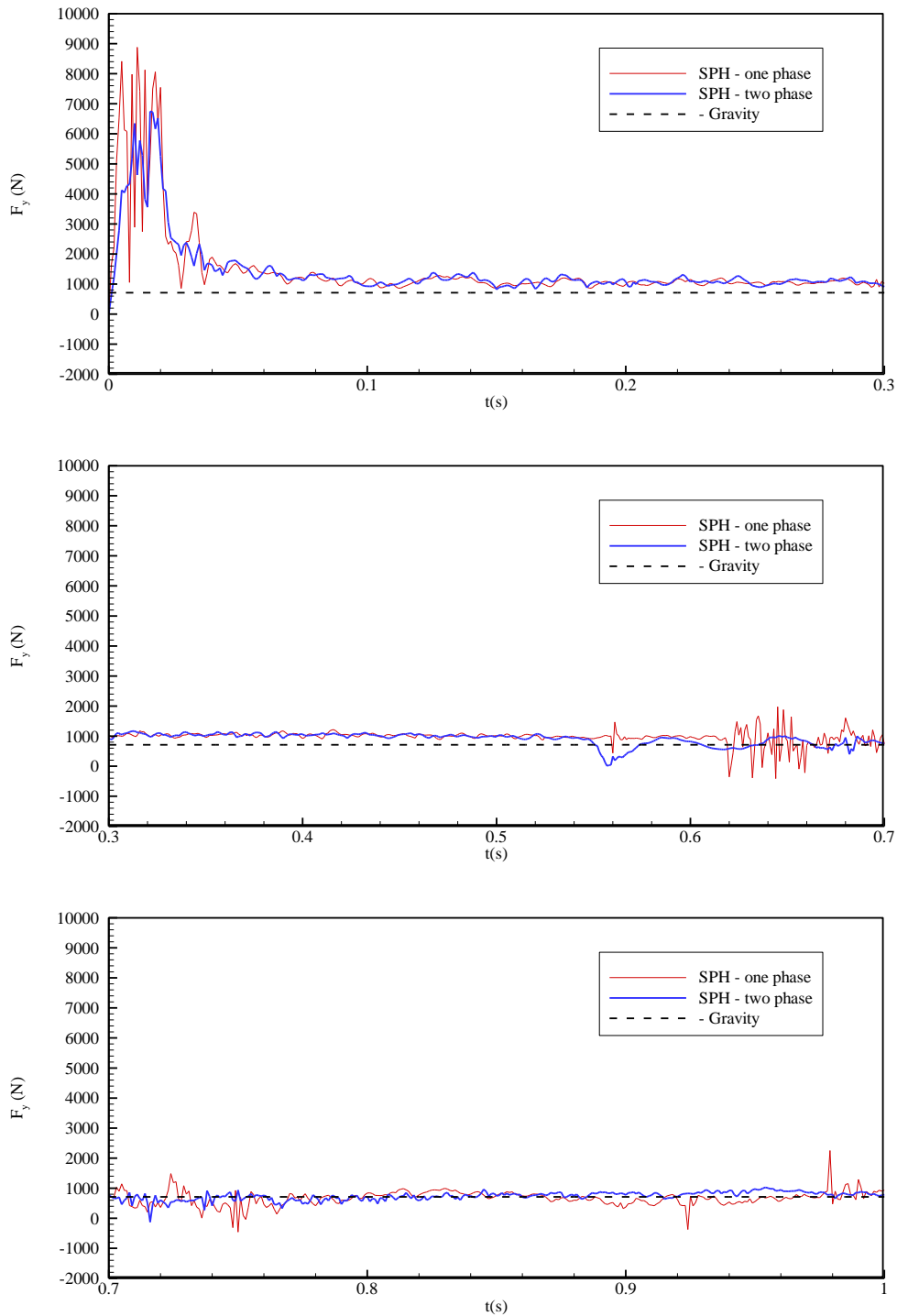
Fig. 18 Time histories of vertical drag forces during the wedge entry (with time axis being split into three continuous segments from up to down)

Two-phase SPH modelling of wedge entry based on laboratory experiment

Since it is not easy to find the data to validate the entire wedge entry process, especially after the air cavity is closed, here we designed a laboratory experiment following the principles of Zhao and Faltinsen (1993) aiming to validate the two-phase SPH computations for the later stage of the wedge kinematics. The experiment was carried out in the MOE Key Laboratory of Hydrodynamics, Shanghai Jiaotong University. The site photo and the schematic setup of the water tank and falling wedge are shown in Fig. 19 (a) and (b), respectively. The water tank is 0.9 m long, 0.32 m wide and 1.8 m high, with the initial water depth of 0.6 m. An iron-made wedge, with a cross-sectional length 0.1 m, dead-rise angle 30° and self-weight 3.444 kg, is dropped at a distance of 0.2 m above the still water surface. The total length of the wedge is 0.3 m, which is shorter than the width of the water tank 0.32 m, so as to ensure no physical contact with the side walls during entry process. According to our experimental analysis on the sidewall effect, the measurement error due to the 3D effect is below 0.5% and thus we could expect a 2D SPH simulation is able to realistically reflect the real 3D experimental conditions. To avoid the damage of the water tank bottom, the wedge is controlled by an iron line of 1.8 m long so the experiment stopped when the wedge is very close to the bottom wall. The whole water entry process was recorded by a high speed video camera Phantom v6.2 with 600 fps. The experiment was terminated after the air cavity region was closed, which lasted for about 0.3 s.
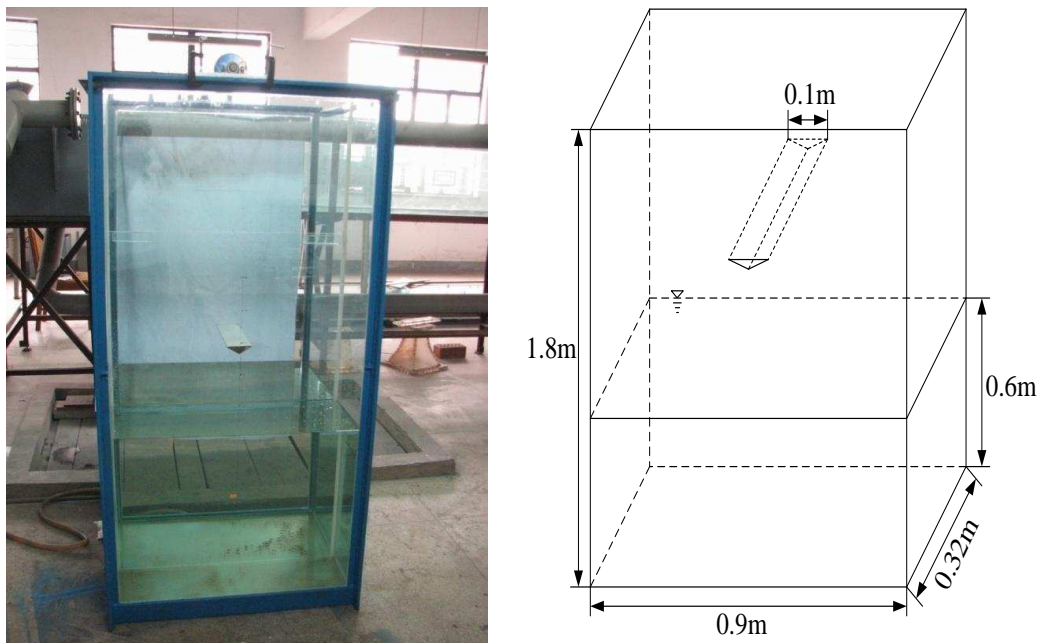
Fig. 19 Water tank and falling wedge used in the laboratory experiment. (a) Site photo; and (b) Schematic view

The experimental photos for the whole wedge entry process are shown in Fig. 20, which demonstrate the formation and closure of the air cavity region as well as the subsequent air region detachment.

t = 0.05 s

t = 0.1 s

t = 0.15 s

t = 0.2 s

t = 0.25 s

t = 0.3 s
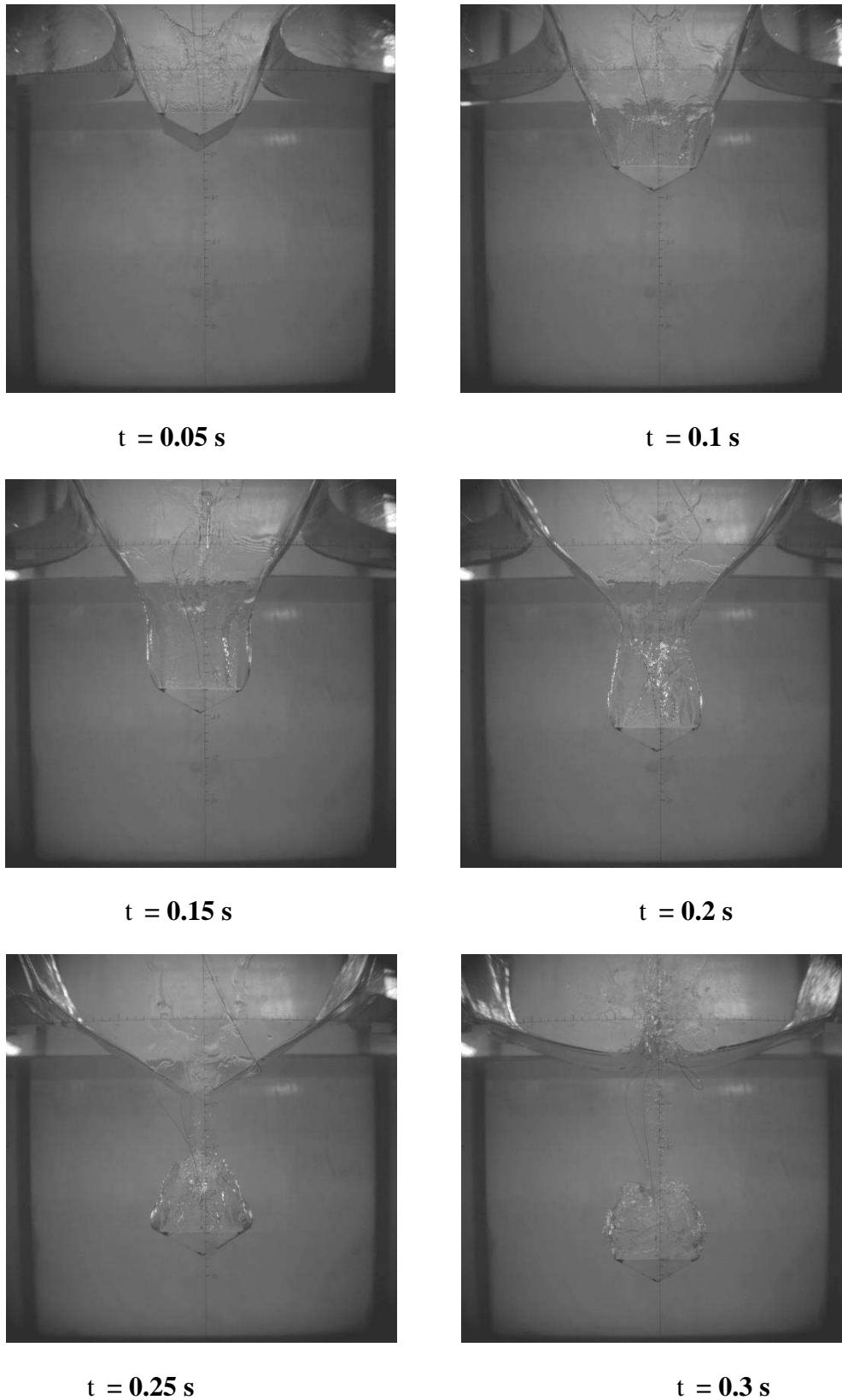
Fig. 20 Laboratory photos of wedge entry process

Now we only use the two-phase SPH model to reproduce the above experiment. The dimension of the computational tank and the wedge is the same as the physical ones, except that the height of the water tank is reduced to 0.975 m to avoid unnecessary CPU cost. In the SPH simulations, the particle distance is $\Delta X = 1.25$ mm and the time step is $\Delta t = 10^{-6}$ s. Thus there are 345,600 water particles and 214,250 air particles in the flow domain. The other computational parameters, such as the viscosity coefficient, XSPH coefficient, EoS constant and background pressure etc, are the same as those used in the previous wedge entry simulations. The total simulation time is 0.3 s. In order to save the computational effort, similar absorbing boundaries as mentioned before (Gong et al., 2009) are also implemented to remove the sound disturbances from the tank wall so that the simulation time can be extended.

Fig. 21 shows the comparisons between the experimental measurement and numerical simulations at two typical time instants, i.e. when the air cavity is closed at t = 0.235 s and when the strong flow jet is generated at t = 0.267s. The black squares on the right column in the numerical results represent the free surface and water-air interface measured from the laboratory experiment. The results in Fig. 21 demonstrate that during the air cavity closure at t = 0.235 s the numerical free surfaces agree with experimental ones very well, except that the experimental cavity location is slightly higher. As the wedge further moves down, two flow jets are generated at t = 0.267 s, which can be clearly seen from the experimental photos. Again, a satisfactory match has been found on the free surfaces but slight underestimations appear in the cavity area. Nonetheless, the shape of the air cavity region has also been satisfactorily reproduced.
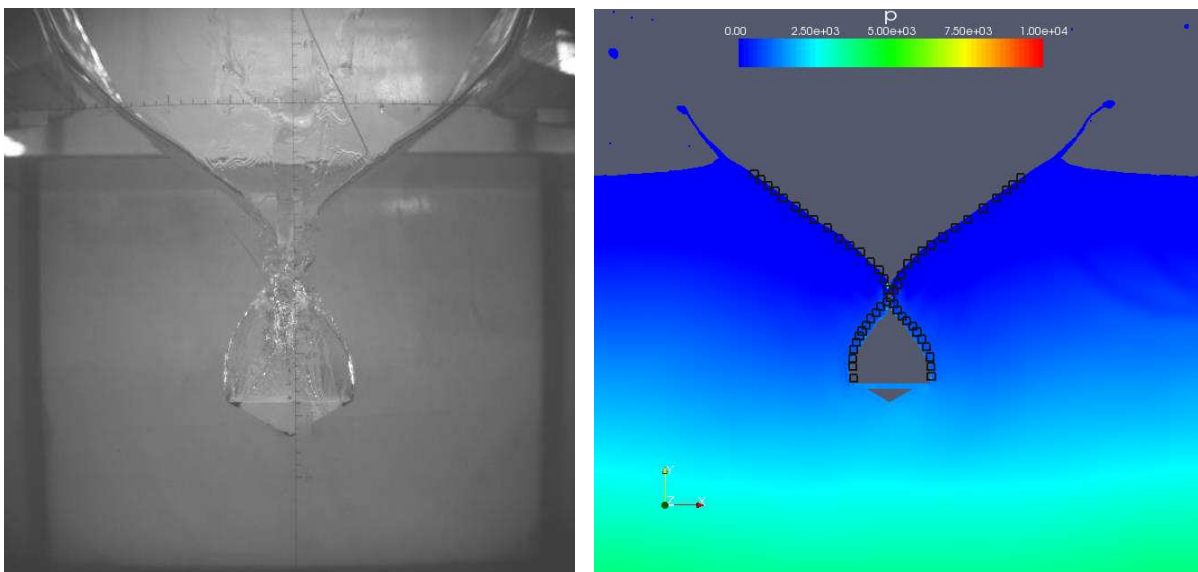
t = **0.235 s**
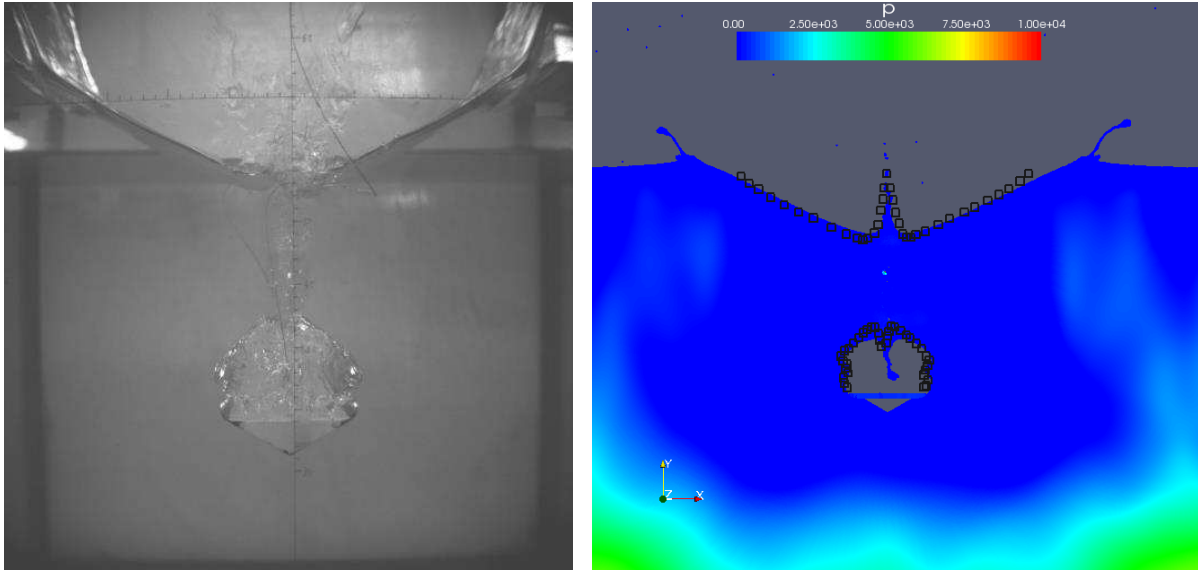
t = **0.267 s**

Fig. 21 Comparisons between experimental (left) and SPH (right) results of air cavity evolution and jet generation (black squares on the right indicate measurement)

Here it is very encouraging to note that the SPH computations can realistically disclose the unevenness on the two lateral sides of the air cavity region. We have found from both the experiment and numerical simulations that during the later stage of the wedge entry, some kinds of turbulence vortex formed near the two wings of the wedge and they gradually moved up and tended to separate from the wedge surface. During this process, the phenomenon of unevenness gradually appeared. We assume this could be due to the non-homogeneous turbulent effect and the SPH particle modelling could capture this naturally even if no explicit turbulence model is used.

Finally, to further demonstrate the robustness of two-phase SPH modelling capacity in the air bubble dynamics, the time evolution features of the air cavity surface are shown in Fig. 22. Also the corresponding close-up experimental photos are provided for a comparison. It shows that immediately after the closure of the air cavity, it shrinks due to the interactions of the neighbouring water pressure. At t = 0.245 s, the bottom width of the air cavity becomes larger than the upper surface area of the wedge. Then the air cavity starts to expand and the pressure inside gradually decreases, so the over-length part of the air cavity above the wedge surface bends upwards due to the fluid pressure, which forms the initial unevenness at t = 0.251 s. As the wedge further moves down, the unevenness develops against the wedge moving direction. Meanwhile, again due to the subsequent shrinking of the air cavity, the dimension of the unevenness region increases until to time t = 0.259 s. Finally the quasi-stable unevenness pattern is formed at t = 0.267 s.
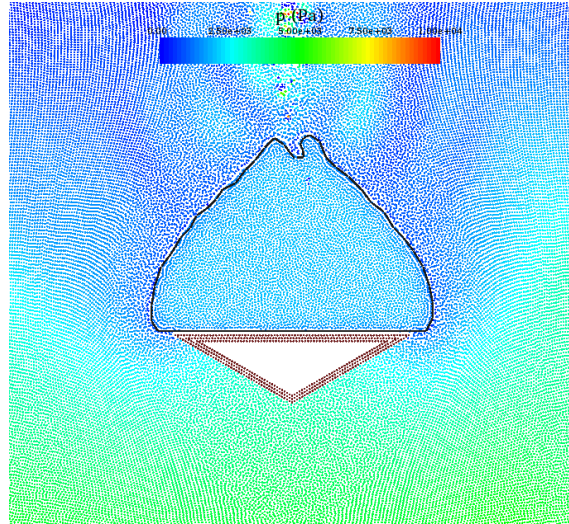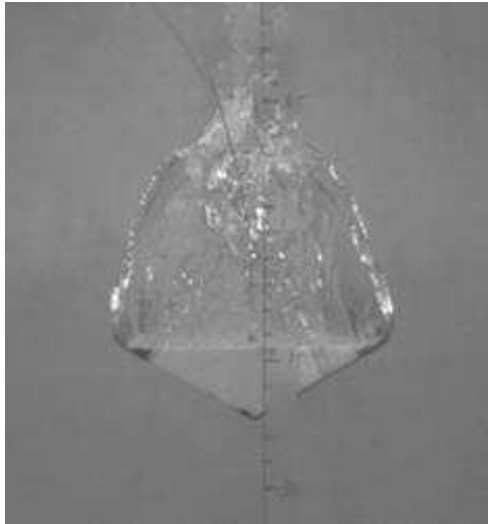
t = **0.245 s**

t = **0.251 s**

t = **0.259 s**

32
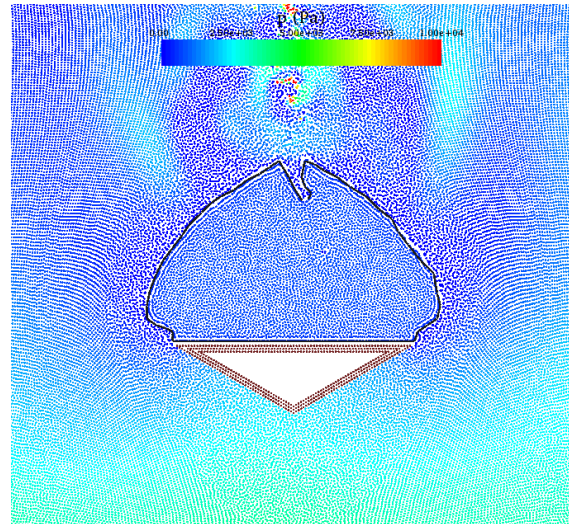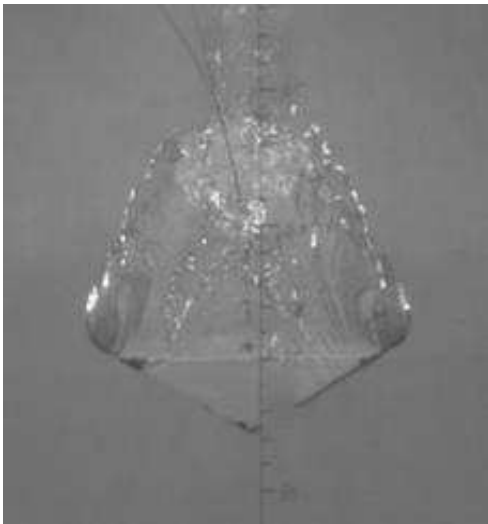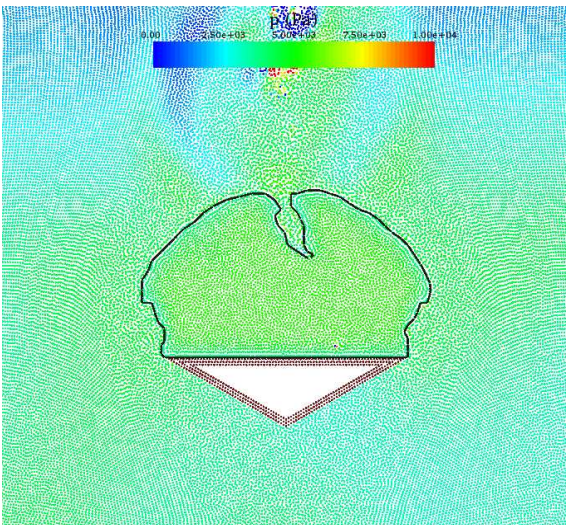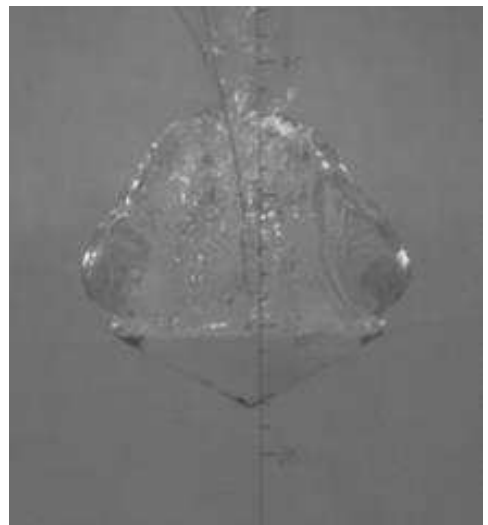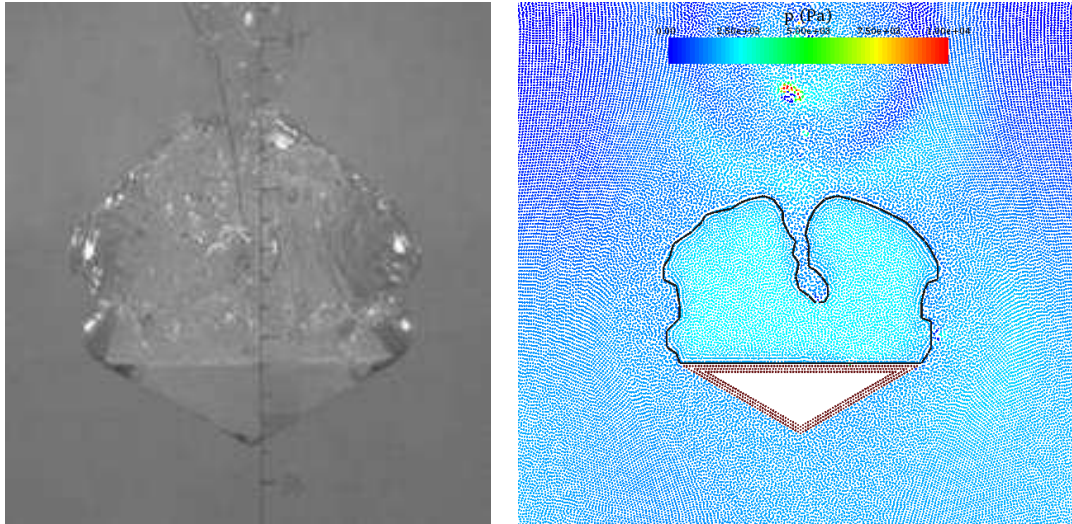
t $= \mathbf{0.267}$ s

Fig. 22 Experimental close-up photos (left) and SPH results (right) on time evolutions of air cavity surface unevenness (black lines on right indicate the water-air interface)

Conclusions

In this paper we carried out the single- and two-phase SPH computations of various fluid-structure interaction problems based on the improved solid boundary treatment. The model applications include the sloshing in a water tank, dam break flow impact on a vertical wall and entire wedge entry process after the air cavity is closed. The model simulations are found to be in good agreement with the documented data. The extended laboratory experiment motivated by Zhao and Faltinsen (1993) validated the shape and dimension of the air bubble entrainment behind the wedge water impact computed by the two-phase SPH model. The unevenness pattern on the lateral bubble surface, which would be difficult to find out by using the mesh-based approaches unless a very high resolution is used, has been well reproduced by the SPH computations using relatively coarse particle spacing. Generally speaking, the proposed two-phase SPH simulations very well predicted the experimental observations on the refined air bubble dynamics, demonstrating the model accuracy and usefulness in the practical water-air interaction problems.

Acknowledgements

References

Chen, Z., Zong, Z., Li, H. T. and Li, J. (2013), An investigation into the pressure on solid walls in 2D sloshing using SPH method, Ocean Engineering, 59, 129-141.

Colagrossi, A. and Landrini, M. (2003), Numerical simulation of interfacial flows by Smoothed Particle Hydrodynamics, Journal of Computational Physics, 191, 448-475.

Colicchio, G., Landrini, M. and Chaplin, J. C. (2003), Level-set modeling of the air-water flow generated by a surface piercing body, Proc. 8th Int. Conf. on Numer. Ship Hydrodynamics, Korea.

Cummins, S. J. and Rudman, M. (1999), An SPH projection method, Journal of Computational Physics, 152, 584-607.

De Leffe, M., Le Touzé, D. and Alessandrini, B. (2009), Normal flux method at the boundary for SPH, Proc. IVth SPHERIC International Workshop, Nantes (France), pp. 149–156.

Dehnen, W. and Aly, H. (2012), Improving convergence in smoothed particle hydrodynamics simulations without pairing instability, Mon. Not. R. Astron. Soc., 425, 1068–1082.

Faltinsen, O. M., Rognebakke, O. F., Lukovsky, I. A. and Timokha, A. N. (2000), Multidimensional modal analysis of nonlinear sloshing in a rectangular tank with finite water depth, Journal of Fluid Mechanics, 407, 201-234.

Ferrand, M., Laurence, D., Rogers, B. and Violeau, D. (2010), Improved time scheme integration approach for dealing with semi-analytical wall boundary conditions in Spartacus2D, Proc. Vth SPHERIC International Workshop, Manchester (UK), pp. 98–105.

Ferrand, M., Laurence, D., Rogers, B., Violeau, D. and Kassiotis, C. (2012), Unified semi-analytical wall boundary conditions for inviscid, laminar or turbulent flows in the meshless SPH method, Int. J. Num. Meth. Fluids, **7**1(4), 446–472.

Gao, R., Ren, B., Wang, G. Y. and Wang, Y. X. (2012), Numerical modelling of regular wave slamming on subface of open-piled structures with the corrected SPH method, Applied Ocean Research, 34, 173-186.

Gingold, R. A. and Monaghan, J. J. (1977), Smoothed Particle Hydrodynamics, Mon. Not. R. Astron. Soc., 181, 375-389.

Gomez-Gesteira, M. G. and Dalrymple, R. A. (2004), Using a three-dimensional Smoothed Particle Hydrodynamics method for wave impact on a tall structure, Journal of Waterway, Port, Coastal and Ocean Engineering, 130, 63-69.

Gong, K., Liu, H. and Tan, S. K. (2011), Numerical simulation of sloshing in 2D rectangular tank based on SPH method with an improved boundary treatment approach, Asian and Pacific Coasts 2011, Dec 14-16, Hong Kong.

Gong, K., Liu, H. and Wang, B. (2009), Water entry of a wedge based on SPH model with an improved boundary treatment, Journal of Hydrodynamics, 21, 750-757.

Gong, K., Wang, B. and Liu, H. (2010), Modeling water entry of a wedge by multiphase SPH method, Proceedings of 32nd International Conference on Coastal Engineering (ICCE), Shanghai, China.

Grenier, N., Antuono, M., Colagrossi, A., Le Touzé, D. and Alessandrini, B. (2009), An Hamiltonian interface SPH formulation for multi-fluid and free surface flows, J. Comput. Phys., 228, 8380–8393.

Hu, X. Y. and Adams, N. A. (2006), A multiphase SPH method for macroscopic and mesoscopic flows, J. Comput. Phys., 213, 844–861.

Hu, X. Y. and Adams, N. A. (2007), An incompressible multi-phase SPH method, Journal of Computational Physics, 227, 264-278.

Huera-Huarte, F. J., Jeon, D. and Gharib, M. (2011), Experimental investigation of water slamming loads on panels, Ocean Engineering, 38(11-12), 1347-1355.

Hwang, S. C., Khayyer, A., Gotoh, H. and Park, J. C. (2014), Development of a fully Lagrangian MPS-based coupled method for simulation of fluid-structure interaction problems, Journal of Fluids and Structures, 50, 497-511.

Koshizuka, S., Nobe, A. and Oka, Y. (1998), Numerical analysis of breaking waves using the moving particle semi-implicit method, International Journal for Numerical Methods in Fluids, 26, 751-769.

Kulasegaram, S., Bonet, J., Lewis, R.W. and Profit, M. (2004), A variational formulation based contact algorithm for rigid boundaries in two-dimensional SPH applications, Comput. Mech., 33, 316–325.

Leroy, A., Violeau, D., Ferrand, M. and Kassiotis, C. (2014), Unified semi-analytical wall boundary conditions for 2-D incompressible SPH, J. Comput. Phys., 261, 106–129.

Leroy, A., Violeau, D., Ferrand, M. and Joly, A. (2015), Buoyancy modelling with incompressible SPH for laminar and turbulent flows, Int. J. Num. Meth. Fluids, 78(8), 455–474.

Lin, P. Z. (2007), A fixed-grid model for simulation of a moving body in free surface flows, Computers & Fluids, 36, 549-561.

Lind, S. J., Stansby, P. K., Rogers, B. D. and Lloyd, P. M. (2015), Numerical predictions of water-air wave slam using incompressible-compressible smoothed particle hydrodynamics, Applied Ocean Research, 49, 57-71.

Liu, M. B., Shao, J. R. and Li, H. Q. (2014), An SPH model for free surface flows with moving rigid objects, International Journal for Numerical Methods in Fluids, 74, 684-697.

Marrone, S., Antuono, M., Colagrossi, A., Colicchio, G., Le Touzé, D. and Graziani, G. (2011), d-SPH model for simulating violent impact flows, Comput. Methods Appl. Mech. Engrg., 200, 1526–1542.

Maruzewski, P., Le Touze, D., Oger, G. and Avellan, F. (2010), SPH high-performance computing simulations of rigid solids impacting the free-surface of water, Journal of Hydraulic Research, SI, 126-134.

Mayrhofer, A., Rogers, B. D., Violeau, D. and Ferrand, M. (2013), Investigation of wall bounded flows using SPH and the unified semi-analytical wall boundary conditions, Comput. Phys. Com., 184, 2515–2527.

Monaghan, J. J. (1994), Simulating free surface flows with SPH, J. Comput. Phys., 110, 399-406.

Monaghan, J. J. and Kocharyan, A. (1995), SPH simulation of multi-phase flow, Computer Physics Communication, 87, 225-235.

Oger, G., Alessandrini, B. and Ferrant, P. (2005), Capture of air cushion effects in a wedge water entry SPH simulation, Proceedings of 15th International Offshore and Polar Engineering Conference (ISOPE 2005), Vol. 3, 241-246.

Oger, G., Doring, M., Alessandrini, B. and Ferrant, P. (2006), Two-dimensional SPH simulations of wedge water entries, Journal of Computational Physics, 213, 803-822.

Ren, B., Jin, Z. and Gao, R. (2014), SPH-DEM modeling of the hydraulic stability of 2D blocks on a slope, Journal of Waterway, Port, Coastal and Ocean Engineering, 140, No. 04014022.

Skillen, A., Lind, S., Stansby, P. and Rogers, B. (2013), Incompressible smoothed particle hydrodynamics (SPH) with reduced temporal noise and generalised Fickian smoothing applied to body-water slam and efficient wave-body interaction, Computer Methods in Applied Mechanics and Engineering, 265, 163-173.

Sussman, M., Smereka, P. and Osher, S. (1994), A level set approach for computing solutions to incompressible two-phase flow, J. Comput. Phys., 114, 146-159.

Vandamme, J., Zou, Q. P. and Reeve, D. (2011), Modeling floating object entry and exit using Smoothed Particle Hydrodynamics, Journal of Waterway, Port, Coastal and Ocean Engineering, 137, 213-224.

Violeau, D. and Issa, R. (2007), Numerical modelling of complex turbulent free-surface flows with the SPH method: an overview, Int. J. Numer. Meth. Fluids, 53, 277–304.

Violeau, D. and Leroy, A. (2014), On the maximum time step in weakly compressible SPH, J. Comput. Phys., 256, 388–415.

Wang, J. and Faltinsen, O. M. (2013), Numerical investigation of air cavity formation during the high-speed vertical water entry of wedges, Journal of Offshore Mechanics and Arctic Engineering – Transactions of the ASME, 135(1), Article Number: 011101.

Wang, J., Lugni, C. and Faltinsen, O. M. (2015), Analysis of loads, motions and cavity dynamics during freefall wedges vertically entering the water surface, Applied Ocean Research, 51, 38-53.

Zhao, R. and Faltinsen, O. (1993), Water entry of two-dimensional bodies, J. Fluid Mech., 246, 593-612.

Zhou, Z. Q., De Kat, J. Q. and Buchner, B. (1999), A nonlinear 3-D approach to simulate green water dynamics on deck, Proceedings of the 7th International Conference on Numerical Ship Hydrodynamics, Nantes.

Appendix

Type-I Chebyshev filter is the most common one among the Chebyshev categories. The amplitude response as a function of the angular frequency ω of the nth-order low-pass filter is defined as:

$$G_n(\omega) = \frac{1}{\sqrt{1 + \varepsilon^2 T_n^2\left(\frac{\omega}{\omega_0}\right)}} \tag{A1}$$

where ε is the ripple factor; ω_0 is the cut-off frequency; and T_n is the Chebyshev polynomial of the nth-order. The pass-band exhibits a ripple behavior, with the ripple determined by the ripple factor ε. The ripple is often given in dB. Referring to William (1985), two signals whose level differs by one decibel have an amplitude (field) ratio of $10^{1/20}$.

A 5th-order Type I Chebyshev low-pass filter has been designed to filter the data noise (Smith, 1997). The filter's passband edge frequency was set as 10 Hz and the stopband edge frequency was 20 Hz. The filter has 1dB of passband ripple. Figure A1 shows the frequency response of the proposed filter. It shows that in the passband (0 ~ 10 Hz), the amplitude is almost 0 which means that the signals will not be affected by this frequency band. Thus the signals only with frequency being larger than 10 Hz will be filtered.
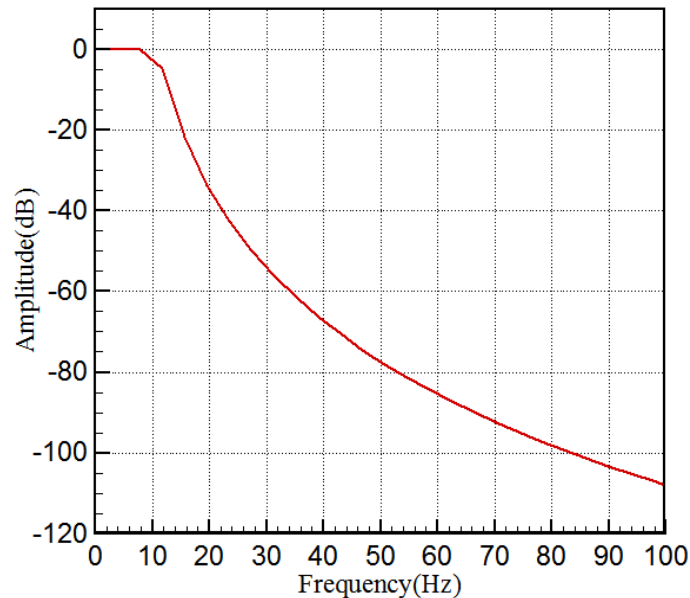
Figure A1. Frequency response of 5th-order Type I Chebyshev low-pass filter

Using this filter to post-process the SPH simulation results, high frequency noises in the pressure data can be effectively filtered. Figure A2 shows the comparison between the original and filtered pressure data for two different external excitation frequencies, based on the sloshing case of Chen et al. (2013) as shown in Figure 6. It shows that the filtering process only removed the data noises but kept the main signals quite well.
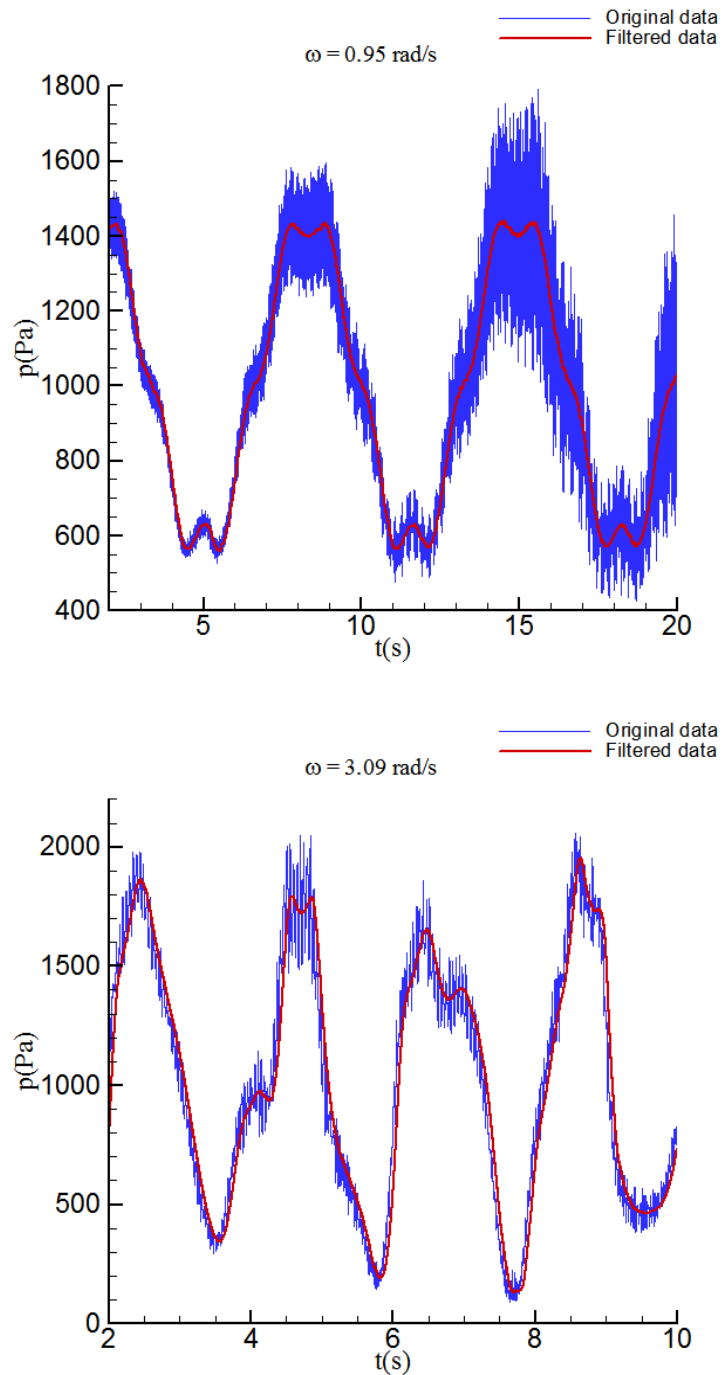
Figure A2. Comparisons between original and filtered pressure data for test case of Chen et al. (2013)

Besides, to investigate the possible links between the pressure data noise and the particle spatial resolution, we also carried out a control run using a finer particle spacing ΔX = 0.0025 m for the sloshing test of Chen et al. (2013), as compared with the original run in which ΔX = 0.005 m was used. The result comparisons in Figure A3 clearly indicate that as the particle number increases, or the particle spacing decreases, the noise level of the pressure data significantly reduces. It should be noted that no data filter was used in Figure A3, which suggests that a higher spatial resolution could help to reduce the numerical pressure noises efficiently as well.
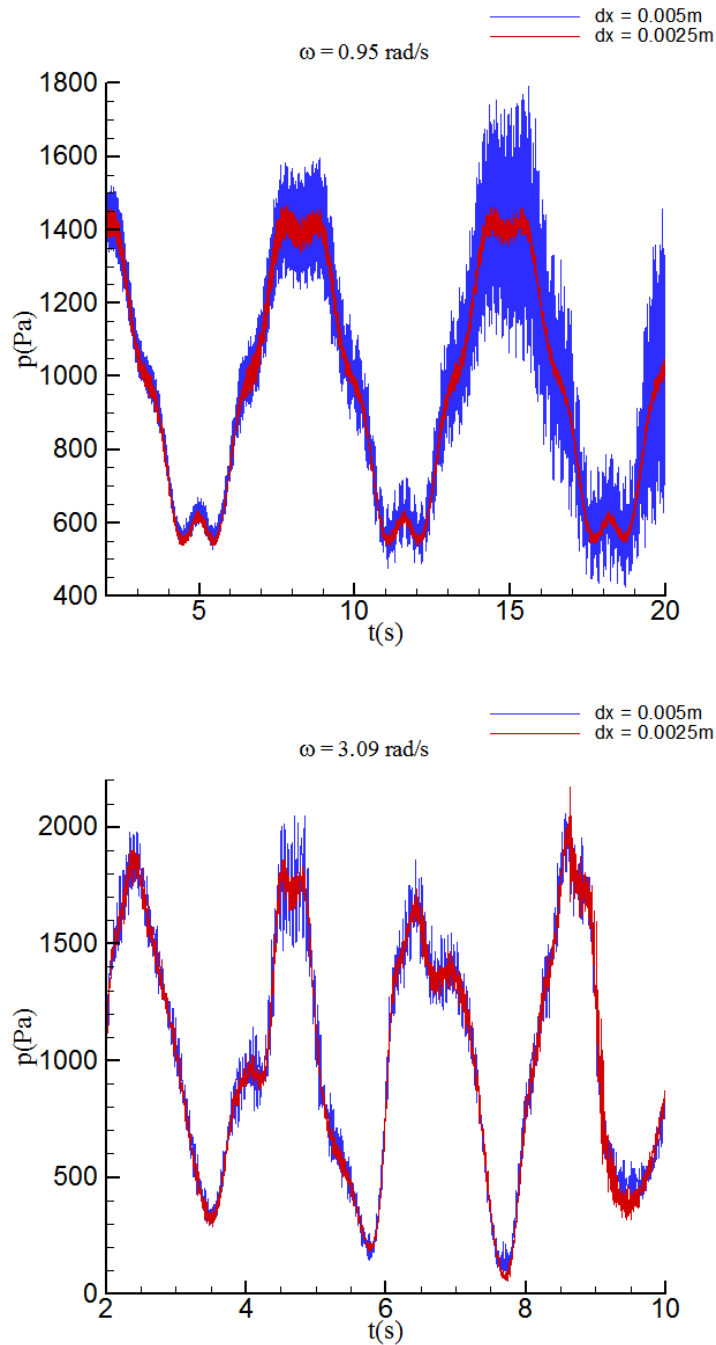
Figure A3. Comparisons between original and refined computations without data filtering for test case of Chen et al. (2013)

References:

Smith, S. W. (1997), The Scientist and Engineer's Guide to Digital Signal Processing, California Technical Pub., pp 333-342.

William, Y. (1985), Fundamentals of Hearing: An Introduction (Second ed.), Holt, Rinehart and Winston, pp 206.